J. Fluid Mech. (1999), *vol.* 391, *pp.* 151–187. Printed in the United Kingdom

Plumes in rotating convection. Part 1. Ensemble statistics and dynamical balances

By KEITH JULIEN[1], SONYA LEGG[2]†, JAMES McWILLIAMS[2] AND JOSEPH WERNE[3]

[1] Department of Applied Mathematics, University of Colorado at Boulder, Boulder, CO 80308-0526, USA

[2] Institute for Geophysics and Planetary Physics, UCLA, Los Angeles, CA 90095-1567, USA

[3] Colorado Research Associates/NWRA, 3380 Mitchell Lane, Boulder, CO 80301, USA

(Received 22 December 1997 and in revised form 11 December 1998)

Atmospheric and oceanic convection often occurs over areas occupied by many localized circulation elements known as *plumes*. The convective transports therefore may depend not only on the individual elements, but also on the interactions between plumes and the turbulent environment created by other plumes. However, many attempts to understand these plumes focus on individual isolated elements, and the behaviour of an ensemble is not understood. Geophysical convection may be influenced by rotation when the transit time of a convecting element is long compared to an inertial period (for example in deep oceanic convection). Much recent attention has been given to the effect of rotation on individual plumes, but the role of rotation in modifying the behaviour of an ensemble is not fully understood. Here we examine the behaviour of plumes within an ensemble, both with and without rotation, to identify the influence of rotation on ensemble plume dynamics.

We identify the coherent structures (plumes) present in numerical solutions of turbulent Rayleigh–Bénard convection, a canonical example of a turbulent plume ensemble. We use a conditional sampling compositing technique to extract the typical structure in both non-rotating and rotating solutions. The dynamical balances of these composite plumes are evaluated and compared with entraining plume models.

We find many differences between non-rotating and rotating plumes in their transports of mass, buoyancy and momentum. As shown in previous studies, the expansion of the turbulent plume by entrainment of exterior fluid is suppressed by strong rotation. Our most significant new result is quantification of the continuous mixing between the plume and ambient fluid which occurs at high rotation without any net changes in plume volume. This mixing is generated by the plume–plume interactions and acts to reduce the buoyancy anomaly of the plume. By contrast, in the non-rotating case, no such loss of buoyancy by mixing occurs. As a result, the total buoyancy transport by upwardly moving plumes diminishes across the layer in the rotating case, while remaining approximately constant in the non-rotating case. At high values of rotation, the net vertical acceleration is considerably reduced compared to the non-rotating case due to loss of momentum through entrainment and mixing and a decelerating pressure gradient which partially balances the buoyancy-driven acceleration of plumes. As a result of the dilution of buoyancy, the pressure-gradient deceleration and the loss of momentum due to mixing with the environment in the

---

† Author to whom correspondence should be addressed, present address: Woods Hole Oceanographic Institution, Woods Hole, MA 02543, USA.

rotating solutions, the conversion of potential energy to kinetic energy is significantly less than that of non-rotating plumes.

The combination of efficient lateral mixing and slow vertical movement by the plumes accounts for the unstable mean temperature gradient that occurs in rotating Rayleigh–Bénard convection, while the less penetrative convection found at low Rossby number is a consequence of the reduced kinetic energy transport. Within the ensemble of plumes identified by the conditional sampling algorithm, distributions of vertical velocity, buoyancy and vorticity mimic those of the volume as a whole. Plumes cover a small fraction of the total area, yet account for most of the vertical heat flux.

1. Introduction

In turbulent convection transport of tracers and heat is effected by intermittent discrete elements often known as plumes. Because they have long lifetimes and move large distances, relative to the Eulerian covariance integral scales of the turbulence, these coherent structures cause non-local, hence non-Fickian material transport across the convective layer. In contrast, many parameterizations of turbulent fluxes are based on local interaction models of the turbulence (e.g. Mellor & Yamada 1982), ignoring the presence of these structures, and result in down-gradient transports. A greater understanding of the structures will enable development of more accurate models of turbulent convective transports.

In a typical geophysical convection context many plumes are generated by a distributed buoyancy source, since the convecting-layer depth is usually thin compared to the spatial scale of lateral variations in the forcing. The net buoyancy and tracer transports by a plume ensemble may differ from those of an isolated element due to interactions between individual elements, yet such ensembles have received little attention thus far. We examine the plume ensemble in numerical solutions of turbulent Rayleigh–Bénard convection, a canonical example of distributed turbulent plume convection, relevant to many geophysical and astrophysical convection scenarios. Plumes are emitted from both upper and lower surfaces of a fluid layer, held at a fixed destabilizing temperature difference. The statistically steady state achieved allows us to identify large numbers of plumes over a long period of time, providing more accurate plume statistics than a time-dependent convecting layer. We concentrate on cases where rotation is strong relative to the buoyancy forcing and compare with non-rotating solutions, in order to identify the role of rotation in the ensemble dynamics. Rotating convection is particularly relevant to geophysical scenarios when the time scale for buoyant elements to traverse the layer is long compared to the inertial period. Our previous work has demonstrated several interesting and important characteristics of low Rossby number convection: the persistence of finite negative temperature gradients, lateral mixing generated by the interaction between cyclonic vortices associated with plumes (Julien *et al.* 1996*a*), less efficient kinetic energy transport and inhibited penetrative convection (Julien *et al.* 1996*b*). Here we will further examine these numerical solutions to quantify the plume structures responsible for these features.

The existence of plumes and their properties in turbulent convection has previously been inferred from examination of their effects on the global transport properties (e.g. the heat flux in the plume-dominated ‘hard turbulent’ regime of high Rayleigh number convection (Castaing *et al.* 1989)). Detailed studies of the budgets of isolated plumes have been carried out in laboratory and numerical investigations (see List 1982 for a review, and Papanicolaou & List 1988 for recent developments). However, the structure of plumes within an ensemble remains difficult to diagnose, the individual elements being elusive and transient, and thus far only geometric properties of plumes (i.e. plume radius) have been identified in distributed forcing scenarios (Maxworthy & Narimousa 1994; Jones & Marshall 1993). Here we will extract the plume structures directly from our previous numerical solutions of turbulent convection, and new simulations using different parameter values, allowing us to evaluate the transport and mixing of properties effected by these structures, as well as their geometric properties. We are motivated in our study by the need for models or parameterizations of convective mixing. Circulation in the oceans, atmospheres, giant planets and stars depends crucially on the convectively driven transports of heat and tracers, yet the scales at which such transports occur are too small to be explicitly modelled if the largest scales are to be captured. Hence, despite increasing computing power, the development of parameterizations remains a fundamental necessity for simulations of these large-scale systems.

We begin by describing the present understanding of turbulent plumes, focusing in particular on the concepts of entrainment and mixing and discussing their modification by strong rotation. Following from these previous studies we outline a modified version of an entraining plume model, incorporating ensemble interactions, to which our solutions will be compared. We then discuss techniques for identifying the coherent structures from the turbulent flow fields, and describe our own method in detail. The structures identified from several different solutions are compared with the entraining plume model, allowing the balances of mass, momentum, and heat to be evaluated. The influence of rotation, Reynolds number and momentum boundary condition in determining the plume transports are quantified.

Our new results include a reduction in net acceleration of rotating plumes, due to both loss of momentum through entrainment and mixing, and a pressure gradient in partial hydrostatic balance with the buoyancy acceleration. Like many previous studies of rotating convection, we find a suppression of plume expansion through entrainment at low Rossby numbers. Our most significant new result, found by evaluation of the heat budget, is the presence of continued mixing as a result of the plume-ensemble generated turbulence which erodes the plume buoyancy in the rotating case, but is absent in the non-rotating case. Since both rotating and non-rotating cases are equally turbulent, this mixing must result from the enhanced lateral motions generated through vortex dynamics in the rotating scenario. This conclusion is supported by observations of large deviations from axisymmetry in rotating plumes, but not in non-rotating plumes. We parameterize this mixing by use of a mixing coefficient, which we find is approximately constant over much of the layer and independent of Reynolds number. Since the turbulence which causes this mixing is generated by the convecting plumes themselves, as is often the case in geophysical scenarios, this mixing coefficient may provide a general parameterization of plume-ensemble interactions in rotating convection. The loss of buoyancy by mixing leads to a reduction in the total heat transport carried by upward moving plumes across the layer in the rotating case. By contrast, the total heat transport carried by upward plumes in non-rotating convection is approximately constant across the layer. (The heat flux carried by downward moving plumes varies in an identical fashion descending through the volume; these Boussinesq solutions are statistically symmetric about the mid-plane.) The reduction in acceleration of the plumes caused by dilution of buoyancy, loss of momentum due to mixing and pressure gradient deceleration, leads to a reduction in the conversion of potential energy to kinetic energy as Rossby number is reduced.

In the present study we ignore many additional features which are present in some of the circulation systems described above: for example, the interaction of plumes with a region of stable stratification, the effects of compressibility and the role of water vapour in atmospheric convection. While such effects are important components of an eventual parameterization scheme, here our emphasis is the modification of plume transports by ensemble interactions and rotation.

2. Buoyant plume models

2.1. *The entrainment hypothesis*

A turbulent buoyant element expands at the expense of the quiescent surrounding fluid through the entrainment of exterior fluid (Morton, Taylor & Turner 1956). This engulfment of exterior fluid by organized structures within the buoyant flow (Papantoniou & List 1989), accompanied by a mixing of ambient tracers and enlargement of the parcel, can be represented by an effective *entrainment velocity* v_e across the parcel bounding surface, defined as the average rate of parcel expansion:

$$v_e = \frac{(\mathrm{d}/\mathrm{d}t)V}{S}, \tag{2.1}$$

where V is the parcel volume, S is the surface area across which entrainment occurs, and $\mathrm{d}/\mathrm{d}t$ is the Lagrangian derivative. Assuming plume tracers are modified only as a result of entrainment into the enlarging turbulent parcel, the parcel motion can be described by

$$\frac{\mathrm{d}}{\mathrm{d}t}V = v_e S, \quad \frac{\mathrm{d}}{\mathrm{d}t}V\overline{W} = V\overline{g'}, \quad \frac{\mathrm{d}}{\mathrm{d}t}V\overline{T} = v_e T_E S, \tag{2.2a–c}$$

where T_E is the temperature of entrained fluid, g' is the parcel buoyancy anomaly, W is the vertical velocity, and T is the parcel temperature. (Note that here and throughout the text we use 'anomaly' to refer to a deviation from the horizontally averaged mean profile.) An overbar represents the average over the parcel, $\overline{X} = (1/V)\int_V X \mathrm{d}V'$. If $v_e = 0$ (an isolated bubble) and a linear relationship between g' and T is specified (e.g. $g' = g\epsilon(T - T_0)$, where ϵ is the coefficient of thermal expansion, and T_0 is the horizontally averaged temperature), a solution for a parcel in a homogeneous environment is

$$W = g\epsilon(T - T_0)t = (2zg\epsilon(T - T_0))^{1/2}, \tag{2.3}$$

the free-fall velocity.

Solutions to the coupled system of equations can be obtained if $v_e \neq 0$ by invoking the entrainment hypothesis (Morton *et al.* 1956), which states that the entrainment velocity is proportional to the vertical velocity:

$$v_e = \alpha\overline{W}, \tag{2.4}$$

where α is a constant, known as the entrainment constant. In addition, a self-similar shape for the element and particular form of forcing must be prescribed.

The *steady plume* model (Turner 1986) results if the buoyant flow is sustained by a continuous source of buoyancy, with entrainment only through the horizontal bounding surface and no time-dependence. Then the Lagrangian derivative above is replaced by the vertical flux gradient $(\mathrm{d}/\mathrm{d}z)W$. For a circular plume in a homogeneous fluid forced by a point source with buoyancy flux F_0, solutions for the radius r, vertical velocity W and buoyancy anomaly g' are

$$r \sim \alpha z, \quad W \sim \left(\frac{F_0}{\alpha^2 z}\right)^{1/3}, \quad g' \sim \left(\frac{F_0^2}{\alpha^4 z^5}\right)^{1/3}, \tag{2.5}$$

where z is the vertical distance from the source.

The *isolated thermal* model results if a buoyant parcel is instantaneously released, without further forcing, and entrainment occurs over the whole surface. For a spherical shape, initial buoyancy $V\overline{g'} = Q$, and homogeneous environment

$$r \sim \alpha z, \quad W \sim \left(\frac{Q}{\alpha^3 z^2}\right)^{1/2}, \quad g' \sim \frac{Q}{\alpha^3 z^3}. \tag{2.6}$$

Both solutions could be obtained from dimensional analysis, assuming self-similar evolution. The use of the entrainment hypothesis and buoyant parcel evolution equations is unnecessary in this case, but in more complicated scenarios such as a plume in a stably stratified environment these equations enable solutions to be obtained (see Emanuel 1994, chapter 1 for numerous examples). Results compare well against observations, demonstrating the utility of the entrainment hypothesis for isolated elements. We intend to investigate the application of the entrainment hypothesis to plume ensembles. Actual convection elements are neither supplied continuously with a source of buoyancy nor released instantaneously, being instead supplied with buoyancy for a finite period of time before detaching from the boundary. We will therefore use the term ‘plume’ to describe any convection element, not just those with a steady source of buoyancy.

2.2. *Rotation and entrainment*

Several recent studies of isolated thermals and plumes under the influence of rotation suggest that the expansion of the element by entrainment can be suppressed when the local Rossby number $Ro_l = u/(fl)$ satisfies the condition $Ro_l < 1$ where u is the velocity scale, f is the Coriolis force and l is the horizontal length scale of the element (Helfrich 1994; Ayotte & Fernando 1994; Fernando & Ching 1993). If the values for $u \sim W$ and $l \sim r$ are inserted from the thermal evolution equations above, then the radius l_{rot} at which this rotational influence occurs is

$$l_{rot} \sim \left(\frac{Q}{f^2}\right)^{1/4}, \tag{2.7}$$

in agreement with laboratory experiments (Helfrich 1994). However, despite the dramatic reduction in expansion when $Ro_l < 1$, the vertical velocity appears unaffected by rotation (Helfrich 1994; Fernando & Ching 1993), contrary to what is predicted from the momentum equation in the absence of entrainment. Possible factors ignored in the self-similar plume and thermal models may be responsible: changes in shape or the modification of vertical acceleration by other terms (apart from buoyancy anomaly), for example pressure drag. An analytical investigation (Bush, Stone & Bloxham 1992) shows that the pressure gradient induced by strong rotation across a buoyant parcel without entrainment can completely balance the buoyancy acceleration. The role of pressure drag in the turbulent case has however not yet been quantified.

2.3. *Plume ensembles*

In the ocean and atmosphere, only a small number of convective features can be described as isolated plumes or thermals (e.g. chimney smoke plumes, hydrothermal vents, waste outflows). Most naturally occurring convection is in the form of ensembles of plumes generated by a distributed buoyancy source (or sink) located at a boundary (Narimousa 1996), introducing several new issues absent from the isolated plume problem: the area between plumes is finite, so that from continuity there must be a return flow between plumes which in turn modifies the environment; the flux of heat into each plume is not known, and may vary with time; the lifetimes of individual plumes are finite and unknown; there may be interactions between plumes (see Ching, Fernando & Davies 1996 for examples of interactions and mergers between two plumes).

Because of these complications, predictions of plume horizontal length, vertical velocity and buoyancy scales have been made through dimensional analysis (e.g. Deardorff 1970), rather than explicit use of the plume equations, giving

$$r \sim z, \quad W \sim (Bz)^{1/3}, \quad g' \sim (B^2/z)^{1/3} \tag{2.8}$$

(where B is the buoyancy flux per unit area: $B = (g\epsilon\mathscr{H})/(\rho_0 C_w)$ where $\mathscr{H}$ is the surface heat loss per unit area, ρ_0 is a reference density and C_w is the fluid specific heat capacity).

As in the single plume and thermal experiments with strong rotation, plume expansion by entrainment is suppressed when the local Rossby number is smaller than a critical value (Fernando, Chen & Boyer 1991; Maxworthy & Narimousa 1994; Jones & Marshall 1993). Using (2.8) to estimate W and r we find the radius (proportional to the depth) at which $Ro_l \approx 1$:

$$l_{rot} \sim \left(\frac{B}{f^3}\right)^{1/2}. \tag{2.9}$$

Maxworthy & Narimousa (1994) and Jones & Marshall (1993) suggest that g' and W must henceforth be independent of depth. A suppression of plume acceleration is then implied, to counteract the continuing buoyancy forcing, but the mechanisms responsible have not been investigated.

2.4. *Detrainment and mixing with the environment*

As well as entraining fluid from the environment, a plume may also lose fluid to the environment (detrainment) or mix properties with the environment without any net change in volume. Priestley (1953) first proposed an ‘open parcel’ model of a plume as a buoyant parcel of constant volume which continuously exchanges heat and momentum with the environment. Then instead of (2.2) we have

$$\frac{\mathrm{d}}{\mathrm{d}t}V = 0, \quad \frac{\mathrm{d}}{\mathrm{d}t}V\overline{W} = V\overline{g'} - k_1 S\overline{W}, \quad \frac{\mathrm{d}}{\mathrm{d}t}V\overline{T} = -k_2 S(\overline{T} - T_E), \tag{2.10a–c}$$

where k_1 and k_2 are turbulent transfer coefficients, representing the rates at which momentum and heat are mixed with the environment. While Priestley examined the properties of plume solutions, and their dependence on the coefficient k_1 and k_2, the value of these coefficients in geophysical convection scenarios was not determined.

Turner (1963) combined the entraining plume with the concept of environmental mixing by introducing detrainment, allowing fluid and plume properties to be lost to the environment. Then the parcel equations (2.2) become

$$\frac{\mathrm{d}}{\mathrm{d}t}V = (v_e - v_d)S, \quad \frac{\mathrm{d}}{\mathrm{d}t}V\overline{W} = V\overline{g'} - Sv_d\overline{W}, \quad \frac{\mathrm{d}}{\mathrm{d}t}V\overline{T} = v_e T_E S - v_d\overline{T}S, \quad (2.11a\text{–}c)$$

where v_d is a detrainment velocity. Note that this model reduces to Priestley's model if $v_e = v_d = k_1 = k_2$. Turner considered solutions where v_d resulted from externally generated turbulence, and showed that it was proportional to the r.m.s. velocity of such turbulence. Turner did not however consider a turbulent convection ensemble as a source of environmental turbulence, or examine the detrainment velocity or mixing coefficient in this case.

2.5. *Plume-based parameterization schemes*

Numerous parameterizations of atmospheric cumulus convection, originating with Arakawa & Schubert (1974), are based on the entraining plume model. Collectively known as mass-flux schemes, they assume the ensemble of plumes behaves much as a collection of isolated plumes. Each grid cell is assumed to contain several plumes, with a distribution of sizes and strengths (and hence effective entrainment rates). Closure schemes are used to determine the initial mass and buoyancy flux at the convective-layer base, invoking for example a large-scale statistical equilibrium (Arakawa & Schubert 1974) or minimization of available potential energy (Fritsch & Chappell 1980). An additional feature of many of these schemes is detrainment or loss of fluid from the plume, either when it reaches neutral buoyancy, as in the two above schemes, or at a constant rate proportional to the entrainment rate (Tiedtke 1989; Gregory & Rowntree 1990). More recent variations on these schemes involve partial mixing with the environment (Kain & Fritsch 1990; Hu 1997), and vertical momentum budgets (Donner 1993). The actual rates of entrainment and detrainment have not been determined explicitly from observations or simulations of detraining plumes.

Recently atmospheric mass-flux schemes have been modified to parameterize ocean convection, with sea-water properties substituted for those of air and water vapour (Paluskiewisz & Romea 1997; Alves 1995). Neither scheme includes the possibility of modification of entrainment at the low Rossby numbers often found in deep ocean convection or has been compared with actual numerical simulations or observations of plume structures.

2.6. *A theoretical framework for examination of plume ensemble dynamics*

While the dynamics of a single steadily forced plume or instantaneously released thermal appears to be well-described theoretically by the entrainment model, many questions remain regarding the behaviour of an ensemble of plumes and the influence of rotation on the ensemble dynamics:

What are the mass and buoyancy fluxes of a plume within the ensemble?

What is the vertical momentum balance for a plume within the ensemble?

What are the entrainment and detrainment behaviours of plumes?

What are the distributions of plume characteristics within an equilibrium ensemble?

What are the effects of plume interactions and environmental rotation?

We will examine these questions in the context of the entraining/detraining parcel model, adapted from Turner's model (2.11) above:

$$\frac{\mathrm{d}V}{\mathrm{d}t} = \oint_S v_e \mathrm{d}S', \qquad (2.12a)$$

$$\frac{\mathrm{d}V\overline{W}}{\mathrm{d}t} = -V\overline{\frac{\partial P'}{\partial z}} + \oint_S w v_e \mathrm{d}S' - \oint_S w \boldsymbol{U} \cdot \mathrm{d}\boldsymbol{S}' + V\overline{g'} + V\nu\overline{\nabla^2 W}, \tag{2.12b}$$

$$\frac{\mathrm{d}V\overline{T}}{\mathrm{d}t} = \oint_S T v_e \mathrm{d}S' - \oint_S T \boldsymbol{U} \cdot \mathrm{d}\boldsymbol{S}' + V\kappa\overline{\nabla^2 T}. \tag{2.12c}$$

V is the parcel volume, and S is the bounding surface of the volume. P is the pressure, normalized by dividing through by ρ. We have subtracted the mean temperature field from both buoyancy and pressure terms so that $\partial\overline{P'}^{0}/\partial z = \partial\overline{P}^{0}/\partial z - g\epsilon T_0$, where $\overline{}^{0}$ denotes azimuthal average and T_0 is the horizontally averaged temperature. Here we have associated a term $\oint_S v_e Q \mathrm{d}S'$ with the change of a quantity Q associated with a change in volume. This could be entrainment $v_e > 0$ or detrainment $v_e < 0$. Another term $-\oint_S Q\boldsymbol{U} \cdot \mathrm{d}\boldsymbol{S}'$, which we will hereafter refer to as the *exchange term*, represents the change in the quantity Q due to exchange between the plume and environment, without any changes in volume (as in Priestley's model for example). Therefore v_e is associated with the velocity of the plume bounding surface, while $\boldsymbol{U}$ is associated with velocity across that surface. Note several differences between these equations and (2.11), in addition to the slightly different distinction between entrainment and mixing. First, we include $-(\partial/\partial z)\overline{P'}$, the anomalous vertical gradient of pressure across the thermal in (2.12*b*), as suggested by the analytical study of Bush *et al.* (1992). Secondly, we include entrainment of momentum through $\oint_S w v_e \mathrm{d}S'$ in (2.12*b*), since in a plume ensemble entrained fluid may also have significant momentum (e.g. from a plume moving in the same or opposite direction). Thirdly, the entrainment velocity v_e is not assumed to be uniform over the whole surface of the parcel, and hence appears inside the integral. Finally, we include the effects of diffusion and friction through the terms $\kappa\overline{\nabla^2 T}$ and $\nu\overline{\nabla^2 W}$. By evaluating the left-hand sides and buoyancy, pressure-gradient and frictional terms directly, we intend to deduce the entrainment and exchange terms. All interaction between the parcel and its environment (and hence with the turbulence generated by other plumes) is included in these two terms. Hence if these terms can be parameterized in terms of the prognostic quantities, the transports effected by the plume ensemble can be represented. The entrainment hypothesis $v_e = \alpha W$ is one example of such a parameterization: we will investigate whether the exchange term can be represented by an exchange velocity $u_x = \alpha_x W$, for example, (where α_x is a constant) and investigate its dependence on rotation rate, and on other properties of the convecting ensemble (e.g. Reynolds number). Note that the entrainment and exchange terms have opposite signs: an expanding plume ($v_e > 0$) is equivalent to fluid flowing into the plume ($U_r < 0$). In addition to evaluating the entrainment and exchange terms, we will examine the importance of the pressure-gradient term and the dominant balances acting on the plumes. Our plumes will be extracted from solutions of turbulent rotating and non-rotating Rayleigh–Bénard convection described below.

3. Turbulent rotating convection: summary of previous results

We have carried out a series of high-resolution numerical simulations of turbulent Rayleigh–Bénard convection under the influence of strong rotation. Parameters of the sub-set of these simulations which we will consider in this study are described in table 1. Results of calculations at constant convective Rossby number (defined as $Ro_c = (Ra/(\sigma Ta))^{1/2} = 0.75$) were described in Julien *et al.* (1996*a*). These calculations were performed at increasing Rayleigh number, up to a maximum of $Ra = 1.78 \times 10^8$, to our knowledge the highest performed in three dimensions. The numerical model,

Run	Rayleigh number Ra	Taylor number Ta	Supercriticality $(Ra-Ra_c)/Ra_c$ S	Rossby number Ro_c	Domain size $L_x \times L_y \times L_z$	Resolution $nx \times ny \times nz$	Boundary conditions
1	2.81×10^7	5.00×10^7	28.43	0.75	$4 \times 4 \times 2$	$192 \times 192 \times 97$	no-slip
2	2.53×10^6	4.50×10^6	12.27	0.75	$4 \times 4 \times 2$	$128 \times 128 \times 65$	no-slip
3	5.63×10^7	1.00×10^8	28.65	0.75	$4 \times 4 \times 2$	$256 \times 256 \times 129$	free-slip
4	5.63×10^6	1.00×10^7	12.56	0.75	$4 \times 4 \times 2$	$192 \times 192 \times 97$	free-slip
5	4.096×10^7	4.55×10^8	8.64	0.3	$4 \times 4 \times 2$	$256 \times 256 \times 129$	no-slip
6	1.024×10^7	0	1024	∞	$12 \times 12 \times 2$	$512 \times 512 \times 97$	no-slip

TABLE 1. Details of the different solutions for which the plumes are analysed.

described in more detail in Julien *et al.* (1996*a*), integrates the three-dimensional incompressible Boussinesq equations, using a pseudo-spectral decomposition in all 3 directions. The number of spectral modes required at a particular Ra is determined by the relevant Kolmogorov scale at each Ra, so that all dynamically active scales are resolved. We found that for constant Ro_c, a scaling regime for the non-dimensional convective heat flux was achieved at high Ra, such that $Nu \sim Ra^{2/7}$ for no-slip upper and lower boundaries, and $Nu \sim Ra^{1/3}$ for stress-free boundaries. The no-slip result is identical to that found for non-rotating turbulent convection (Heslot, Castaing & Libchaber 1987). However, other quantities show significant differences from non-rotating convection. In particular, with rotation, even at asymptotically high Ra, a finite vertical gradient in the horizontally averaged temperature persists in the convective layer, as in Fernando *et al.* (1991) and Klinger & Marshall (1995). We have suggested that this temperature gradient is a consequence of plume–plume interactions induced by the cyclonic vortices associated with plumes in the presence of rotation, which diminish the buoyancy transports of the plumes by introducing an efficient lateral mixing mechanism. To examine in more detail the plume evolution of these solutions, we will examine the budgets of plumes identified from four of the solutions described in our earlier work. These solutions are identified as runs 1 to 4 in the table. For each type of boundary conditions we include two simulations at different Ra, so as to examine the influence of increasing Reynolds number on the plume dynamics. To examine the influence of rotation on the plume dynamics we also include one simulation with $Ro_c = 0.3$ (run 5) and one without rotation (run 6) in the present study. Both of these calculations have $Ra > 1 \times 10^7$, as in the higher-Ra $Ro_c = 0.75$ simulations, so that turbulence is equally well developed.

In addition to examining the role of plume dynamics in determining the temperature gradients, we will also examine the plume budgets of momentum and consequences for kinetic-energy transport. Our previous studies of the influence of rotation on penetrative convection (Julien *et al.* 1996*b*) have shown that a reduction in kinetic-energy transport at strong rotation leads to a reduction in reverse buoyancy flux in the stratified region bounding a convective layer. Here we will examine plume processes responsible for the kinetic-energy transport reduction.

4. Coherent structure identification

We extract the thermal plume structure from the full flow field by employing a conditionally sampled compositing technique. The state vector for a typical flow structure is obtained by compositing all those sample structures which satisfy a predetermined selection criterion (e.g. updraughts or downdraughts: Schumann & Moeng 1991; Schmidt & Schumann 1989). Attention is focused on a localized region by restricting the size of sample state vectors relative to the full state vector of the flow field. An alternative coherent structure identification technique is the proper orthogonal decomposition (POD) (Lumley 1971; Berkooz, Holmes & Lumley 1993), which obtains a series of characteristic functions describing principal structures of the flow by calculating the eigenvectors of the ensemble-averaged covariance matrix. While POD identifies preferred global patterns of variability (Aubrey *et al.* 1988), it is inadequate to identify highly localized plume or vortex structures (Wilson 1996). An intermediate method conditionally samples to obtain samples focused on a small spatial extent and then carries out a POD. However, the results are almost identical to the conditionally sampled composite, provided one pattern dominates the samples, yet require considerably more effort to obtain. Hence conditional composites appear to be the method best suited to the identification of localized structures such as plumes; this is the approach we pursue.

The composite structure can be highly sensitive to the selection threshold (Yuan & Mokhtarzadeh-Dehghan 1994); we will use a two-step process to reduce this dependence. We intend to focus on the plume evolution or life-cycle and therefore separate the samples in terms of their age or height in the convecting layer, in contrast to previous studies of the coherent structures of convection.

To identify plumes we first recognize that a plume is associated with a distinct signature in both vertical velocity and temperature fields – a hot updraught or a cold downdraught – and also in the vorticity field for convection with ambient rotation. Three fields therefore form our plume state vector: vertical velocity W, temperature anomaly $T - T_0(z)$ (where T_0 is the horizontally averaged temperature) and vertical vorticity ω_3. Since in Boussinesq Rayleigh–Bénard convection there is a symmetry between updraughts and downdraughts, plume structure can be adequately studied by focusing on plumes travelling in one direction only. Hence we concentrate on hot updraughts. Interaction between plumes travelling in the opposite direction will be inferred from the plume budgets.

An initial identification of plumes is made using a strong selection criterion in one field F (where F represents one of temperature, vertical velocity, or vertical vorticity): a three-dimensional local maximum combined with a value $F > \Gamma F_{rms}$ where Γ is a constant and F_{rms} is the root-mean-square value. The location of such a maximum in F is the *plume centre*. The local plume state vector $\boldsymbol{Y}(n)$ is constructed by azimuthally averaging the fields about the plume centre, over a radius $L_x/6$ and a depth $L_z/4$, equally distributed above and below the centre. (L_x and L_z are the horizontal and vertical extents of the computational domain, with $L_x = 2L_z$ for most of our calculations.) The plume state vectors with plume centres at the same vertical level are then combined to obtain the composite azimuthally averaged plume:

$$\langle \boldsymbol{Y} \rangle(z) = \frac{1}{N_1(z)} \sum_{n}^{N_1(z)} \boldsymbol{Y}_n(z), \tag{4.1}$$

where $N_1(z)$ is the total number of plumes identified at the vertical level z over all time for which data are available.

We now repeat the conditional sampling with a greatly relaxed selection criterion – a horizontal maximum in F and a much lower threshold value of F (e.g. $F > 0$). Large numbers of plumes are selected in this way. Each azimuthally averaged state vector $\boldsymbol{X}(n)$ is compared with the previously calculated composite plume $\langle \boldsymbol{Y} \rangle$ at the same vertical level z by calculating the normalized scalar product γ_n where

$$\gamma_n = \frac{\langle \boldsymbol{Y} \rangle \cdot \boldsymbol{X}_n}{(\langle \boldsymbol{Y} \rangle \cdot \langle \boldsymbol{Y} \rangle)^{1/2} (\boldsymbol{X}_n \cdot \boldsymbol{X}_n)^{1/2}}. \tag{4.2}$$

If $\gamma_n > \gamma_k$ where γ_k is a predetermined threshold value, $\boldsymbol{X}_n$ is retained in the subset for further compositing. In this way a subgroup of plumes is created, selected by their *structure* (i.e. correlation between fields or spatial distribution of anomalies) and not by amplitude.

Since a typical plume has several local horizontal maxima in F (due to both the finite vertical extent of the plume and the small-scale structure within the plume), there will be considerable redundancy. This redundancy is eliminated using a further selection criterion: the relative distance between plumes in the vertical $z_{i,j} = |z(i) - z(j)|$ and horizontal $r_{i,j} = ((x_i - x_j)^2 + (y_i - y_j)^2)^{1/2}$ where (x_i, y_i, z_i) are the plume centre coordinates i (as selected by the $F > 0$ criterion). If $r_{i,j} < R_k$ and $z_{i,j} < Z_k$ where R_k and Z_k are predetermined threshold values, the plume centres correspond to local maxima in the same structure. Only the structure with the greater value of γ_n is retained for further compositing.

Finally, having made the plume selection by the three above criteria – local horizontal F maximum, comparison with the previous composite $\langle \boldsymbol{Y} \rangle$, and spatial separation from other plumes – we combine all plumes found at the same z level, to generate a new composite:

$$\langle \boldsymbol{X} \rangle (z) = \frac{1}{N_2(z)} \sum_{n}^{N_2(z)} \boldsymbol{X}_n(z), \tag{4.3}$$

where $N_2(z)$ is the total number of plumes which satisfy all three criteria above. At this stage, in addition to the three fields used in the selection process, we evaluate all other fields and their correlations, and evaluate the composite plume fields over the whole fluid depth, rather than the restricted depth range used to determine the selection of individual plumes. Our final result is independent of the original selection threshold value Γ. We stratify the structures by vertical level, so that the evolution in structure as an intermittent plume traverses the volume can be identified.

Here we describe the sensitivity of the final composite structure to the adjustable parameters: F, the field to which the selection criterion is applied; Γ, the threshold value of this field (compared to the r.m.s.); γ_k, the threshold value of the state-vector dot product with the first composite; and R_k and Z_k, the minimum horizontal and vertical separation respectively. We calculated composites using vertical velocity, temperature and vertical vorticity as the selection criteria F, and varying Γ, the threshold value. The resultant composite plumes were then compared by calculating the normalized scalar product of the plume state vectors $\boldsymbol{a} \cdot \boldsymbol{b} / ((\boldsymbol{a} \cdot \boldsymbol{a})^{1/2} (\boldsymbol{b} \cdot \boldsymbol{b})^{1/2})$.

The choice of vertical velocity or temperature anomaly maxima as the selection field makes little difference to the resultant plume structure, with a normalized scalar product of greater than 0.9. Vertical vorticity reverses sign as the plume traverses the box, so a vertical vorticity maximum criterion only produces good agreement with the other selection criteria in the lower part of the volume. The structure shows little sensitivity to the value of Γ, although larger values reduce the number of plumes in the sample. Temperature as a selection criterion also results in fewer plumes than vertical velocity. For this reason, vertical velocity maxima, with a threshold value of $\Gamma = 1$ were chosen for production. There is minimal sensitivity to the choice of

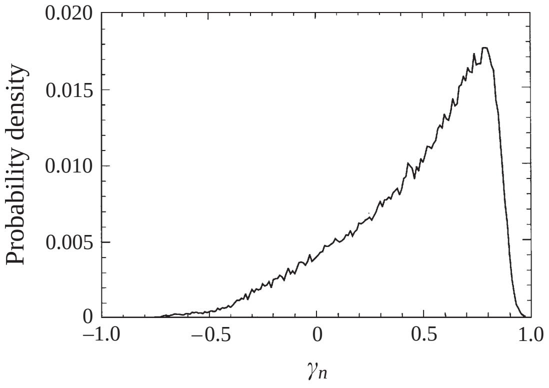

FIGURE 1. The p.d.f. of the normalized scalar product γ_n between all plumes identified by a local horizontal maximum in w, with $w > 0$, and the first composite plume. $Ro_c = 0.75$, $(Ra - Ra_c)/Ra_c = 28.43$, no-slip boundary conditions.

threshold in the second step, where $F > 0$ is used, since the choice of γ_k and R_k and z_k are the controlling parameters in this stage.

The probability density function of γ_n for all the plumes found by the weak $F > 0$ and local maximum threshold shows a peak at higher values, of around 0.8 for all solutions (figure 1). We chose to use $\gamma_k = 0.7$ in order to include all the plumes within this peak, and therefore the most typical structures of the ensemble.

The number of plumes selected depends little on the vertical cutoff distance Z_k, once it is greater than a few grid points. As the horizontal cutoff distance R_k is increased, the isolated plumes tend to show higher correlations with the ideal – a compromise distance is chosen by examining the average width of plumes in each simulation and using this plume width to specify R_k.

5. Results

We have extracted plumes from the different solutions described in table 1, allowing us to examine the sensitivity of plume structure to three different parameters: the Reynolds number $Re = wl/\nu$; the convective Rossby number $Ro_c = (Ra/(Ta\ Pr))^{1/2}$ and the momentum boundary conditions at the upper and lower surfaces. We examine in particular $Ro_c = \infty$, 0.75 and 0.3 and no-slip and stress-free boundary conditions. By examining the momentum, heat and mass budgets of rotating plumes and comparing with the non-rotating case, we will show the following: rotating plumes are in gradient-wind balance, but not in hydrostatic balance; entrainment rates are rapidly suppressed in rotating plumes; modification of properties of rotating plumes is affected by exchange with the environment, with no volume changes; and acceleration of rotating plumes is suppressed, as the buoyancy forcing is balanced by a combination of pressure gradients and loss of momentum to the ambient flow.

5.1. *Typical plume structure in rotating convection: fields and Eulerian budgets for run 1*

We first examine the structures from one solution in the Eulerian frame to identify the dominant balances in the plume flow: e.g. the possibility of geostrophic and/or hydrostatic balance, and the relative important of advective versus diffusive transports. This solution has an *a priori* convective Rossby number (Julien *et al.* 1996*a*) of $Ro_c =$

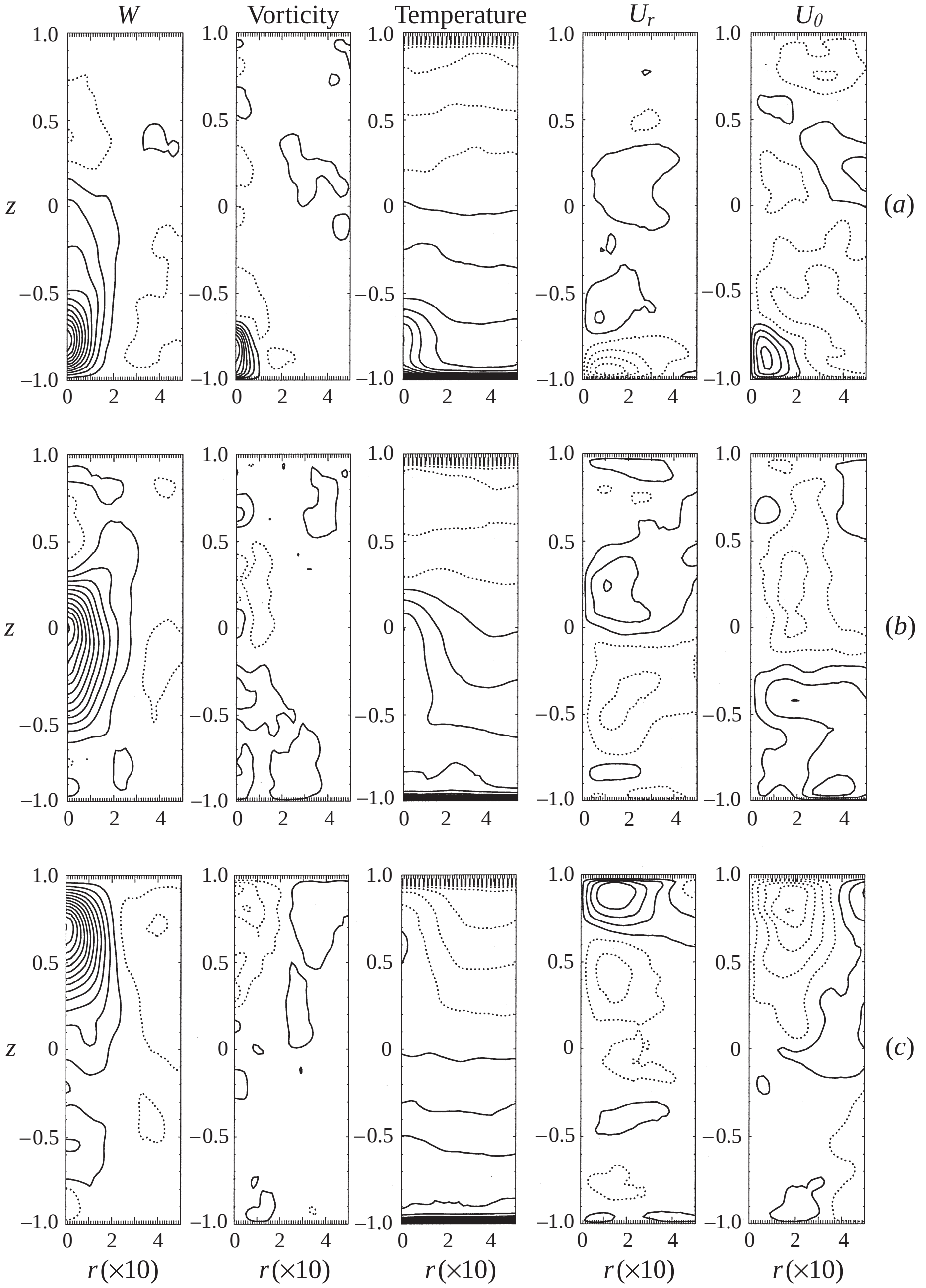

FIGURE 2. The vertical velocity, vorticity, temperature and azimuthal and radial velocity fields for the azimuthally averaged composite plumes centred at heights (*a*) $L_z/8$, (*b*) $L_z/2$ and (*c*) $7L_z/8$ above the bottom boundary. $Ro_c = 0.75$, $(Ra - Ra_c)/Ra_c = 28.43$, no-slip boundary conditions. Contour intervals are: $\Delta W = 38.5\kappa/L$, $\Delta\omega = 0.35f$, $\Delta T = 1/15\delta T$, $\Delta U = 22.2\kappa/L$, where κ is the diffusivity, $2L$ is the layer depth, f is the planetary rotation, and $\delta T = (T_{\text{bottom}} - T_{\text{top}})/2$ is half the temperature difference across the layer. In this and subsequent contour plots, positive values are shown by solid contours and negative values by dotted contours.

$(Ra/(Ta\ Pr))^{1/2} = 0.75$, where Ra is the Raleigh number, Ta is the Taylor number, and Pr is the Prandtl number. This solution (run 1 in table 1) has supercriticality $(Ra - Ra_c)/Ra_c = 28.43$, where Ra_c is the critical Raleigh number for convection to occur at this value of Ta (Chandrasekar 1961) and lies in the turbulent scaling regime. Momentum boundary conditions at top and bottom are no-slip. Figure 2 shows the vertical velocity W, temperature T and vertical vorticity ω_3 of the azimuthally averaged composites, over the full depth of the volume. Since the selection of plumes was determined using the fields over a limited depth, less weight should be placed on those features far above or below the plume centre. Fields at large radii from the plume centre also tend to be noisier, as variability within the ensemble of samples is most evident here. Hence the reader should focus attention principally on features near the plume axis.

We show the full temperature field, as opposed to the temperature anomaly $T - T_0$ used in the selection process, since the full temperature field is necessary for calculation of heat budgets. The vertical velocity maximum is associated with a warm temperature anomaly. Plumes close to the bottom boundary layer are associated with a strong cyclonic vortex, located slightly below the velocity maximum. At higher levels, the strength of this vortex diminishes, and the anticyclonic vorticity component above the vertical velocity maximum increases, as divergence of the flow dominates. Detachment of the plume from the boundary and localization of the structure in the vertical are indicated in both vertical velocity and temperature fields. However, this apparent localization may result from the tilt of plumes away from vertical alignment, and should not be taken to indicate that parcels are completely isolated from their source at the bottom boundary. If plumes are tilted from the vertical, azimuthal averaging may lead to a spurious impression of detachment from the boundary – this tilt is quantified in a later section.

The azimuthal velocity field is baroclinic, reversing flow direction at about the level of the plume (figure 2) like the vorticity signal. There is radial inflow below the plume and outflow above. Inflow is especially strong when the plume is close to the lower boundary, with similarly strong outflow near the upper boundary. Since the azimuthal velocity and vorticity fields are generated by the movement of fluid before and after the thermal, they are less localized in the vertical than other fields.

5.1.1. *Momentum budget*

We examine the relative importance of the terms in the azimuthally averaged vertical momentum budget

$$\frac{\partial}{\partial t}\overline{W}^{\theta} = -\frac{\partial}{\partial z}\overline{P'}^{\theta} - \overline{\nabla\cdot(\boldsymbol{U}W)}^{\theta} + \overline{g'}^{\theta} + \nu\nabla^2\overline{W}^{\theta}, \tag{5.1}$$

where $\overline{}^{\theta}$ is the azimuthal average. If the plume is in hydrostatic balance then the pressure gradient and buoyancy terms will cancel. In figure 3 we show $\overline{g'}^{\theta} = g\epsilon\overline{T'}^{\theta}$, $-(\partial/\partial z)\overline{P'}^{\theta}$ and their residual $\overline{g'}^{\theta} - (\partial/\partial z)\overline{P'}^{\theta}$. Deviation from hydrostatic balance is largest in the boundary layers, where the mean pressure gradient is balanced by inertial terms. However, in the region of the plume, the pressure gradient partially compensates the buoyancy anomaly. This pressure deceleration reduces the net acceleration of the plume. The buoyancy forcing dominates however so this hydrostatic balance is not complete.

Figure 3 shows that the residual buoyancy forcing is small compared to the vertical advection. Frictional drag is small compared to all other terms in the vertical

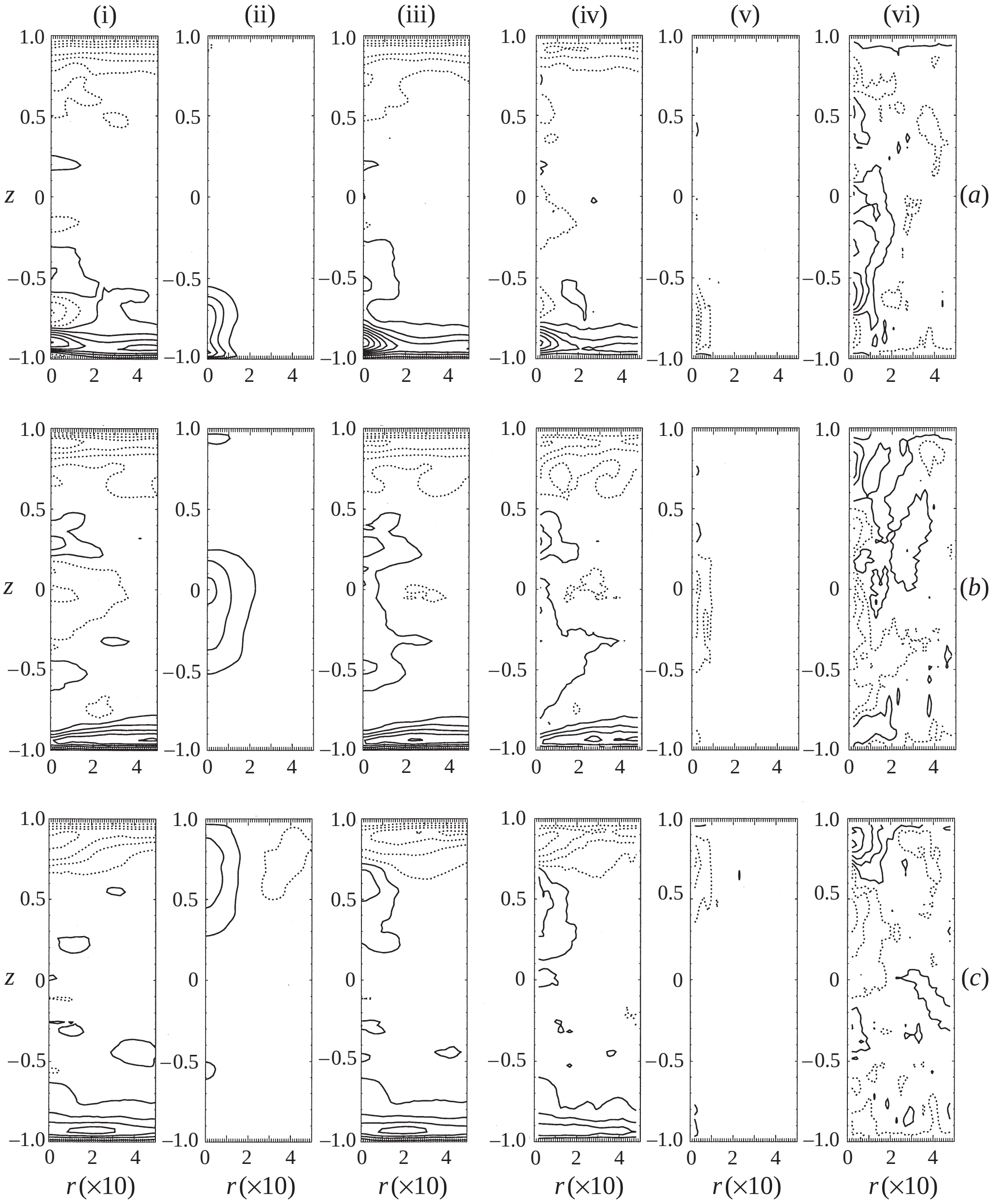

FIGURE 3. The pressure gradient, buoyancy, advective, and diffusive components of the vertical momentum budget for plumes centred at heights (*a*) $L_z/8$, (*b*) $L_z/2$ and (*c*) $7L_z/8$ above the bottom boundary. (i) $-\partial P'/\partial z$, (ii) $g' = g\epsilon(T - T_0)$, (iii) $g' - \partial P'/\partial z$, (iv) $(\partial/\partial z)(W^2) + (1/r)(\partial/\partial r)(rU_rW)$, (v) $\nu\nabla^2 W$, (vi) Residual $= g' - \partial P'/\partial z + \nu\nabla^2 W - (\partial/\partial z)(W^2) + ((1/r)(\partial/\partial r)(rU_rW)) = \partial W/\partial t$. Contour interval = (i–iii) 117 000 κ^2/L^3, (iv) 148 000 κ^2/L^3, (v) 59 100 κ^2/L^3.

momentum balance and confined to the plume axis. In the boundary layer pressure gradients are balanced by the advection terms. In the plume area the dominance of the advection terms leads to an acceleration ahead of the plume, with deceleration behind. In this Eulerian frame it is difficult to identify any changes in the parcel momentum itself which could be caused by entrainment of ambient fluid, since these are masked by the parcel advection.

5.1.2. *Heat budget*

A similar examination of the relative importance of the terms in the azimuthally averaged heat budget

$$\frac{\partial}{\partial t}\overline{T}^{\theta} = -\overline{\nabla \cdot (\boldsymbol{U}T)}^{\theta} + \kappa \nabla^2 \overline{T}^{\theta} \tag{5.2}$$

shows that radial inflow fluxes heat into the plume, while the outflow transports heat outwards (figure 4), leading to warming below the plume and cooling above in lower layers. Along the upper boundary, the radial flow leads to a net warming. Vertical transports by contrast lead to cooling below the plume and warming above the plume, until close to the upper boundary, when the vertical heat fluxes become negligible. The vertical transports dominate, so the net advective effect is cooling below the plume and warming above, consistent with the upward transport of a localized warm anomaly. Near the boundaries, diffusion balances advection, but within the plume core the diffusive cooling is comparatively small. Net changes in the plume-area temperature field are therefore dominated by advection. As in the momentum budget, it is not possible to identify changes in the parcel heat content induced by entrainment in this Eulerian frame.

5.1.3. *Gradient-wind balance*

If the azimuthally averaged fields are in gradient-wind balance, then

$$\frac{\partial \overline{P'}^{\theta}}{\partial r} = f\overline{u_\theta}^{\theta} + \frac{\overline{u_\theta^2}^{\theta}}{r}, \tag{5.3}$$

making no assumptions about hydrostatic balance, since we have shown this does not hold (and therefore not assuming ‘thermal wind balance’, which uses the hydrostatic relation to substitute for pressure in terms of temperature in the vertical derivative of (5.3)). Figure 5 shows that in the interior of the volume the pressure gradient is approximately balanced by the Coriolis and centrifugal terms (with the centrifugal term typically about 20% the magnitude of the Coriolis term). Significant deviations from gradient-wind balance occur only in the Ekman boundary layers where radial inflows (at the bottom boundary layer) or outflows (in the top boundary layer) are generated.

5.2. *Lagrangian plume budgets: comparisons between different simulations*

In the Eulerian frame we found that the convection elements are somewhat localized in the vertical, and in gradient-wind balance with partial hydrostatic balance between the buoyancy and pressure gradient anomalies (although the buoyancy forcing always dominates). Advection dominates both the heat and momentum budgets in the Eulerian frame. The Lagrangian frame of reference moving with the parcel allows us to separate the modification of heat and momentum by entrainment and mixing from parcel advection. We will therefore compare plume budgets in different simulations within the Lagrangian frame indicated in (2.12*a–c*).

5.2.1. *Plume shape and size*

Our examination of the Lagrangian budgets may be simplified if the thermals have self-similar shapes during their evolution. We therefore examine the vertical

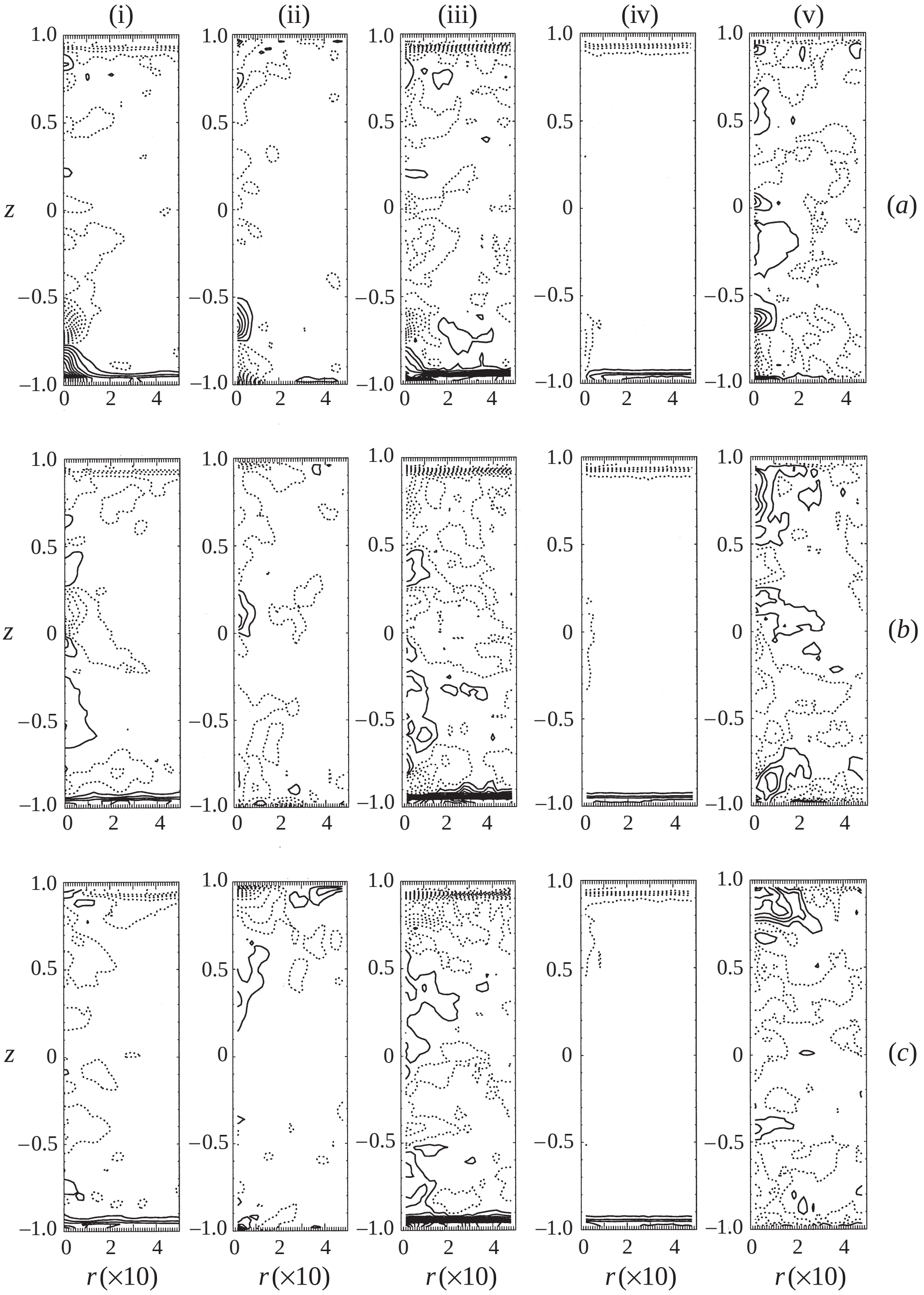

FIGURE 4. The advective and diffusive components of the heat budget for plumes centred at heights (*a*) $L_z/8$, (*b*) $L_z/2$ and (*c*) $7L_z/8$ above the bottom boundary. (i) $(\partial/\partial z)(WT)$, (ii) $(1/r)(\partial/\partial r)(rU_rT)$, (iii) $(\partial/\partial z)(WT) + (1/r)(\partial/\partial r)(rU_rT)$, (iv) $\kappa\nabla^2 T$, (v) Residual $= \kappa\nabla^2 T - ((\partial/\partial z)(WT) + (1/r)(\partial/\partial r)(rU_rT)) = \partial T/\partial t$. Contour spacing is (i), (ii), (iv) $101\delta T\kappa/L^2$, and (iii), (v) $40.6\delta T\kappa/L^2$.

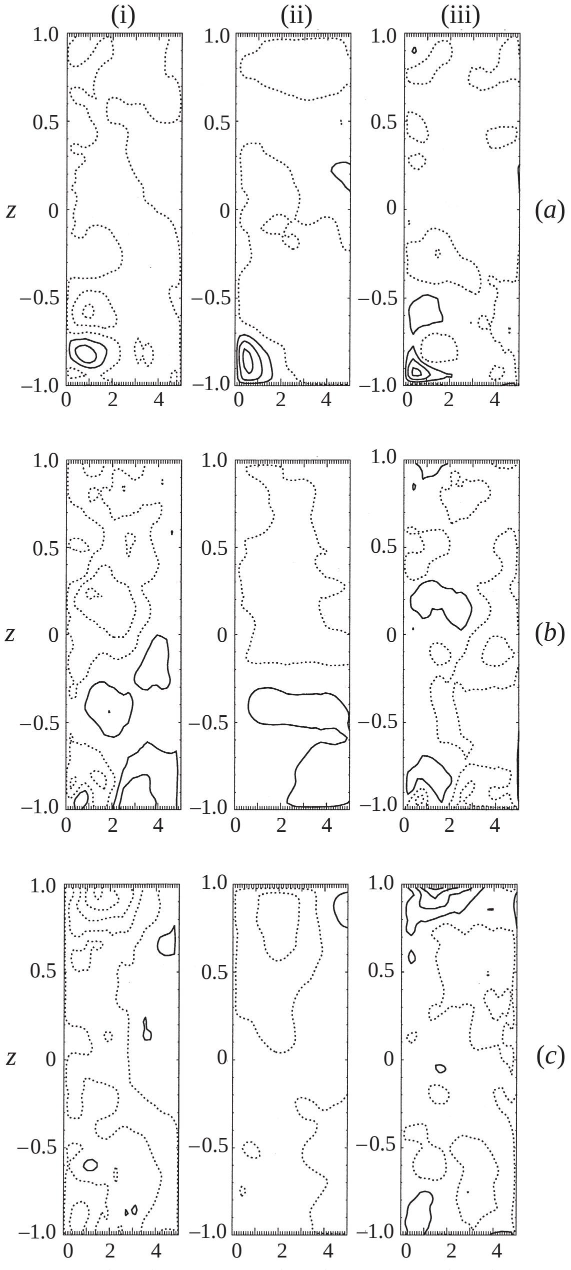

Figure 5. The terms in the gradient-wind balance for plumes centred at heights (*a*) $L_z/8$, (*b*) $L_z/2$ and (*c*) $7L_z/8$ above the bottom boundary. (i) The radial pressure gradient, scaled by the density $(\partial P/\partial r)/\rho_0$, (ii) the Coriolis and centrifugal terms $fu_\theta + u_\theta^2/r$, and (iii) the residual $fu_\theta + u_\theta^2/r - (\partial P/\partial r)/\rho_0$. Contour interval = $75644\ \kappa^2/L^3$.

velocity shape in both radial and vertical directions, for run 1. Shown in figure 6(*a*) are comparisons between the velocity field at the central level of a plume as a function of the radius, for all stages in the plume evolution. The velocity field is scaled by its maximum value at the plume centre and compared with (*a*)

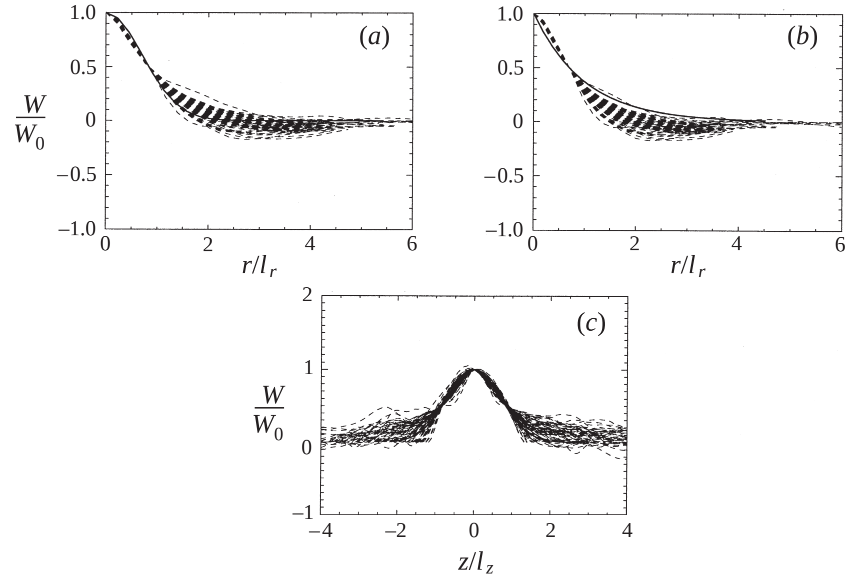

FIGURE 6. The vertical velocity field W for all composite plumes in run 1 (each different plume-centre height corresponding to a different dashed line), scaled by the maximum value W_0 at that plume-centre height. (*a*) $W(r)/W_0$ as a function of scaled radial distance, r/l_r, at the central level of all composite plumes compared to a Gaussian function $W = W_0 \exp(-r^2/l_r^2)$ (solid line); (*b*) $W(r)/W_0$ compared to an exponential function; $W = W_0 \exp(-r/l_r)$ (solid line); (*c*) $W(z)/W_0$ along the vertical axis of the plume, as a function of scaled vertical distance z/l_z compared to a Gaussian function (solid line), where l_z is estimated separately above and below the plume centre.

a Gaussian fit $W_0 \exp(-r^2/l_r^2)$ where l_r is estimated from the half-width distance, $l_r = r_{1/2}/(\ln(2.0))^{1/2}$; and (*b*) an exponential fit $W_0 \exp(-r/l_r)$ where $l_r = r_{1/2}/\ln(2.0)$. The shape lies consistently between a Gaussian and exponential decay. A similar pattern is found for the temperature field. Non-rotating isolated plumes show a similar Gaussian radial profile (Papanicolaou & List 1988). In the vertical direction (figure 6*b*), the decay of the vertical velocity field appears to be more Gaussian, but different decay scales apply above and below the plume centre. Since the shapes are relatively self-similar, but with length scales that vary both in z and in the spatial direction from the plume centre, we will define the plume volume as that region within the surface defined by the vertical velocity half-width, i.e. where $W < W_0/2$. The plume thus defined will have a shape which may vary with height. We do not assume it to be spherical or ellipsoidal.

The self-similarity of the plume radial shape with height allows us to characterize the fields by a measure of the decay scale in both horizontal and vertical directions, and the averaged value over the volume defined by the three-dimensional decay lengths. We choose $r_{1/2}$, the distance at which the vertical velocity is equal to half of its maximum, as the horizontal length scale, and $h_{1/2} = z_{+1/2} - z_{-1/2}$, the difference between the half-width distances above and below the plume centre, as the vertical length scale.

Shown in figure 7 are the radius $r_{1/2}$, and vertical length $h_{1/2}$ for the different solutions, as a function of the plume-centre height. The plumes have much greater vertical extent than horizontal radius, with both increasing rapidly initially, indicating enlargement of the plume by entrainment. However, in strongly rotating cases, over the interior of the layer both vertical extent and radius remain approximately constant,

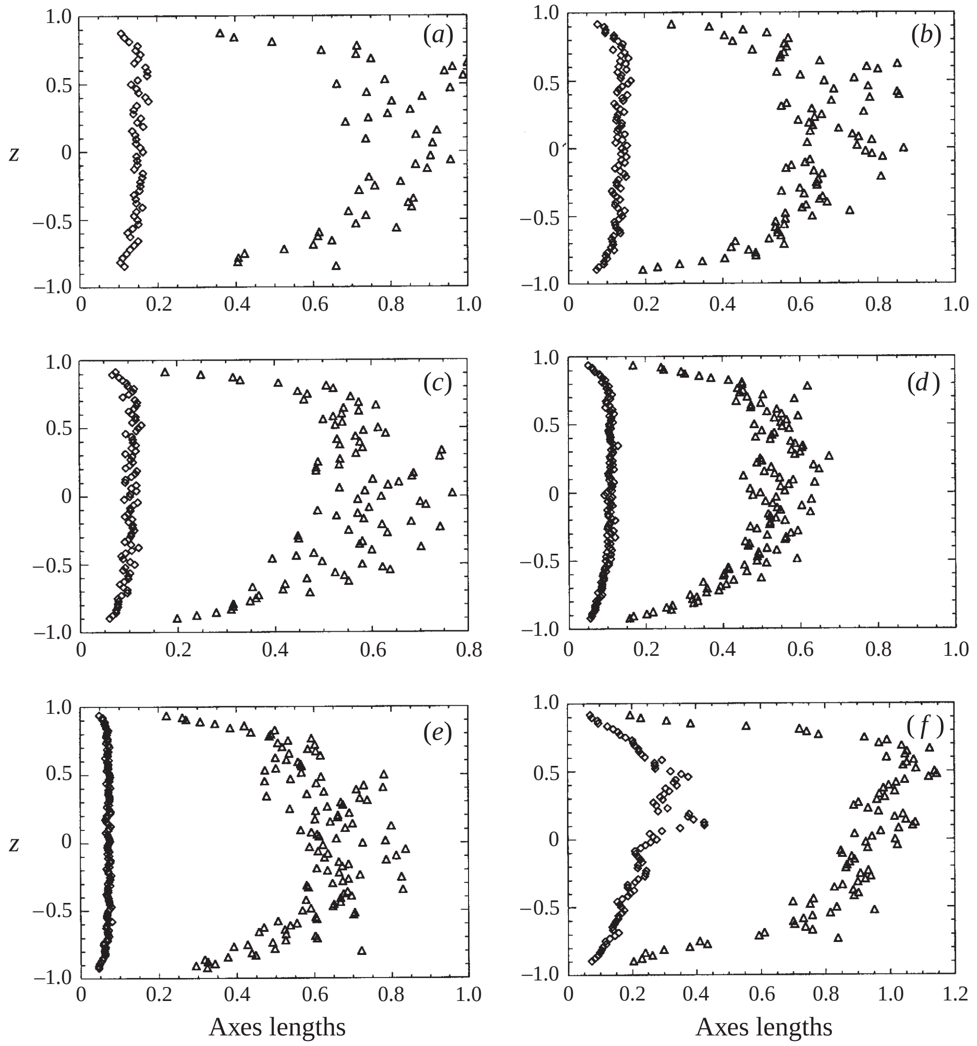

FIGURE 7. The radius (diamonds) and length (triangles) of plumes for six simulations of different Rossby number Ro_c, supercriticality S, and boundary conditions. (*a*) $S = 12.27$, $Ro_c = 0.75$, no-slip; (*b*) $S = 12.56$, $Ro_c = 0.75$, stress-free; (*c*) $S = 28.43$, $Ro_c = 0.75$, no-slip; (*d*) $S = 28.65$, $Ro_c = 0.75$, stress-free; (*e*) $S = 8.64$, $Ro_c = 0.3$, no-slip; (*f*) $S = 1024$, $Ro_c = \infty$, no-slip. These runs are identified as runs 2, 4, 1, 3, 5, 6 respectively in table 1.

indicating a suppression of entrainment. In contrast, the non-rotating plumes continue to expand with $r \sim z$ (as for isolated plumes, Papanicolaou & List 1988). The resultant plume volume reflects this suppression of entrainment in rotating cases, and continued expansion in the non-rotating case. This suppression of entrainment in rotating plumes is shown in previous studies (Fernando *et al.* 1991; Maxworthy & Narimousa 1994; Helfrich 1994), which suggest that entrainment is suppressed once the local Rossby number is sufficiently reduced. To verify this hypothesis we calculate the local Rossby number $Ro_l = \overline{W}/(f \times 2r)$ where r is the thermal radius at the height of the thermal centre (figure 8). The higher-Ra $Ro_c = 0.75$ solutions show a Ro_l which is initially > 1. Ro_l then decreases (due to entrainment) to a value < 1, and close to the *a priori* estimation of the convective Rossby number Ro_c, whereupon it remains constant

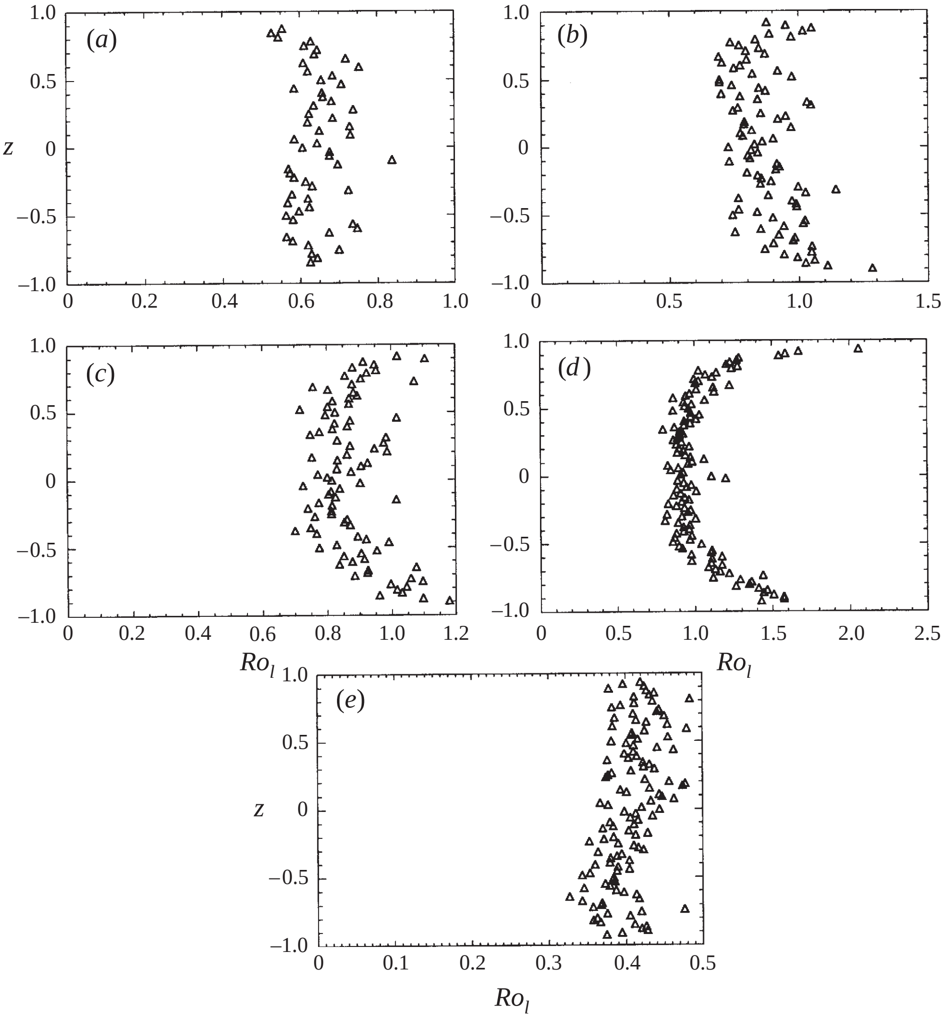

FIGURE 8. The local Rossby number $Ro_l = \overline{W}/(f2r)$ for five different simulations. (*a*) $S = 12.27$, $Ro_c = 0.75$, no-slip; (*b*) $S = 12.56$, $Ro_c = 0.75$, stress-free; (*c*) $S = 28.43$, $Ro_c = 0.75$, no-slip; (*d*) $S = 28.65$, $Ro_c = 0.75$, stress-free; (*e*) $S = 8.64$, $Ro_c = 0.3$, no-slip. These runs are identified as runs 2, 4, 1, 3, 5 respectively in table 1.

over the rest of the layer. This supports the hypothesis that entrainment is reduced when $Ro_l < 1$. The higher Rossby numbers in the boundary layers correspond to the small plume radii in these regions: plume expansion then reduces the Rossby number. $Ro_c = 0.3$ shows no boundary layer enhancement, perhaps indicating that the scale at which rotation controls the flow and suppresses expansion is very close to the scale at which plumes are ejected from the boundary layer.

5.2.2. *Evaluation of balances*

To evaluate the relative components of the Lagrangian budgets, we replace $\mathrm{d}/\mathrm{d}t$ by $(\mathrm{d}/\mathrm{d}z)W$ since our composites are sorted by vertical height rather than time. We then integrate the quantities WT, W^2, W, $\nabla^2 T$, $\nabla^2 W$, $\partial P'/\partial z$, and g' over the volume contained within the ellipsoid defined by the surface $W = W_0/2.0$. Calculation of the gradients of the first three quantities with plume height enables the missing terms in

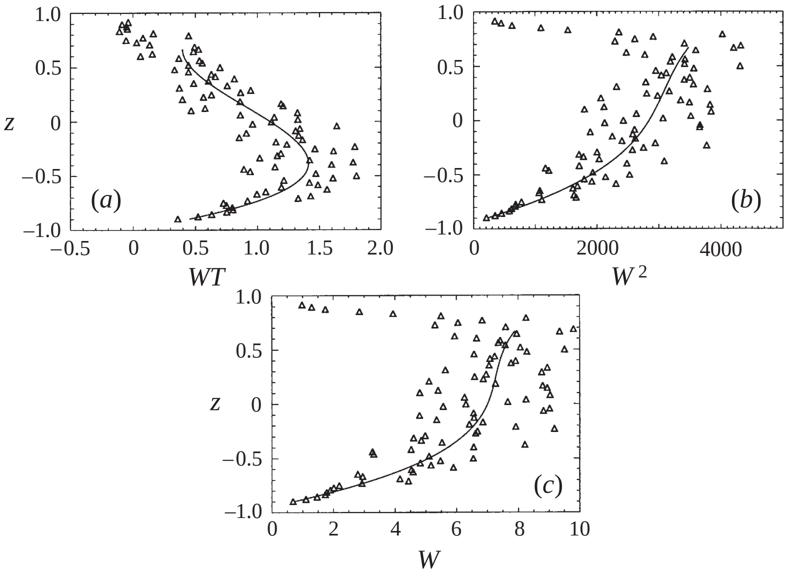

FIGURE 9. Quantities integrated over the whole plume volume V as a function of height of the plume centre, for $Ro_c = 0.75$, $(Ra - Ra_c)/Ra_c = 28.43$ and no-slip boundary conditions (run 1). Also shown are the best fourth-order-polynomial fits to these quantities, from which the first derivatives will be calculated. (*a*) $V\overline{WT}/(\kappa\delta T L^2)$, (*b*) $V\overline{W^2}/(\kappa^2 L)$, (*c*) $V\overline{W}/(\kappa L^2)$.

the conservation equations to be estimated. These quantities ($V\overline{WT}$, $V\overline{W^2}$ and $V\overline{W}$) are shown in figure 9 as a function of the plume-centre height, along with the best fourth-order-polynomial fit, from which the first derivative is calculated (for run 1). The polynomial fit is evaluated only in the interior, avoiding the boundary layers where the plumes are formed and destroyed.

The heat equation

Terms in (2.12*c*) are shown in figure 10. In rotating cases, over much of the interior the change in the vertical heat flux $(\mathrm{d}/\mathrm{d}z)(V\overline{WT}) \equiv (\mathrm{d}/\mathrm{d}t)(V\overline{T})$ is negative, implying loss of heat as the parcel progresses in the vertical. This change is much greater in magnitude than can be accounted for by the small loss due to diffusion. Since entrainment is small in the interior (see below), exchange of heat with the surrounding fluid, $-\oint_S T\boldsymbol{U}\cdot \mathrm{d}\boldsymbol{S}'$, must be responsible. In contrast, the vertical heat flux continues to increase across the layer in the non-rotating case, with implications for the implied exchange coefficient (see below).

The vertical momentum equation

The vertical momentum flux equation (2.12*b*) in figure 11 also shows significant differences between the rotating and non-rotating cases. In rotating cases, the acceleration $(\mathrm{d}/\mathrm{d}z)(V\overline{W^2}) \equiv (\mathrm{d}/\mathrm{d}t)(V\overline{W})$ is greater than the buoyancy forcing $V\overline{g'}$ near the bottom boundary, and smaller than the buoyancy term in the interior. In contrast, in the non-rotating case, the net acceleration is larger than the buoyancy forcing through much of the layer, decreasing only as the opposite side of the layer is approached. With rotation, the reduction in acceleration over much of the layer is due in part to a partial hydrostatic balance between the buoyancy anomaly and the vertical pressure gradient anomaly (which is about 1/3 the magnitude of the buoyancy anomaly). The rest of the deceleration is provided by the residual which we associate with

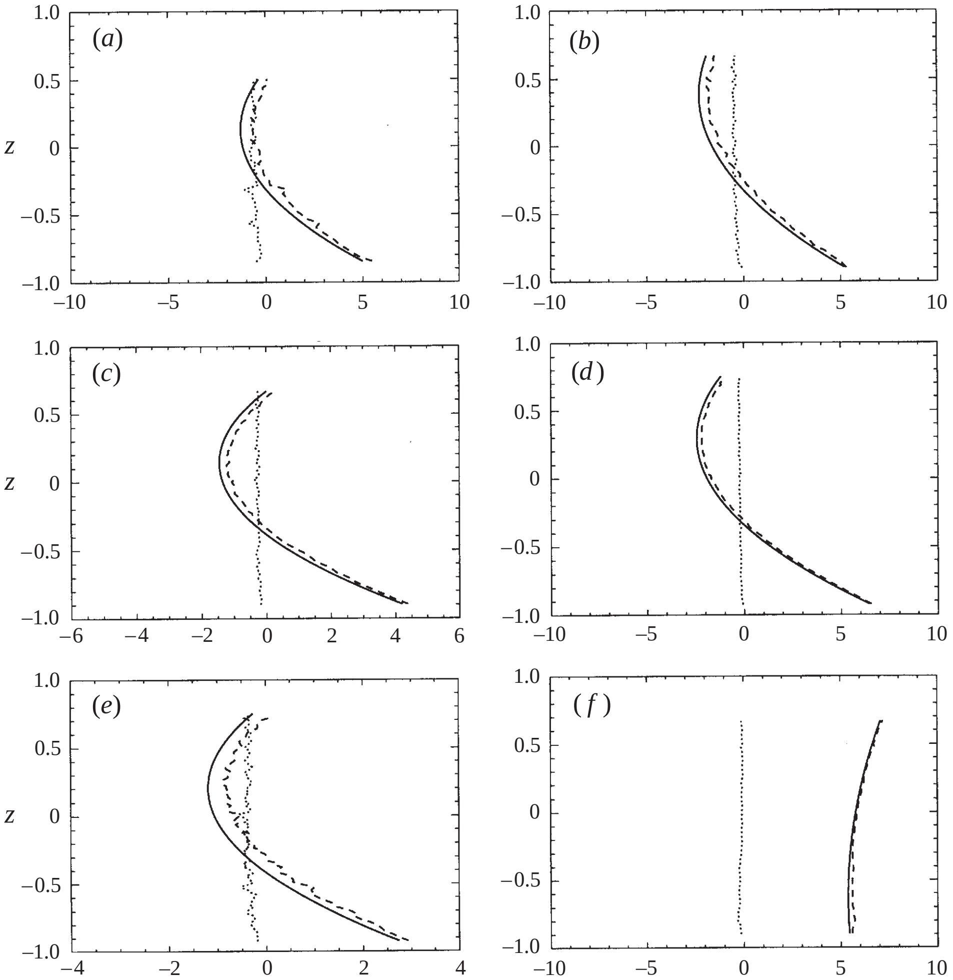

FIGURE 10. The components of the Lagrangian heat balance for six simulations of different Rossby number Ro_c, supercriticality S, and boundary conditions. (*a*) $S = 12.27$, $Ro_c = 0.75$, no-slip; (*b*) $S = 12.56$, $Ro_c = 0.75$, stress-free; (*c*) $S = 28.43$, $Ro_c = 0.75$, no-slip; (*d*) $S = 28.65$, $Ro_c = 0.75$, stress-free; (*e*) $S = 8.64$, $Ro_c = 0.3$, no-slip; (*f*) $S = 1024$, $Ro_c = \infty$, no-slip. These runs are identified as runs 2, 4, 1, 3, 5, 6 respectively in table 1. The different terms shown are: solid line = $(\mathrm{d}/\mathrm{d}z)(V\overline{WT}) \equiv (\mathrm{d}/\mathrm{d}t)(V\overline{T})$, dotted line = $V\kappa\nabla^2\overline{T}$ and dashed line is the residual $(\mathrm{d}/\mathrm{d}z)(V\overline{WT}) - V\kappa\nabla^2\overline{T}$ which we equate with $\oint_S Tv_e dS' - \oint_S T\mathbf{U}\cdot\mathrm{d}\mathbf{S}'$. All quantities are non-dimensionalized by $\kappa\delta TL$.

entrainment and exchange: $\oint_S wv_e\mathrm{d}S' - \oint_S w\boldsymbol{U}\cdot\mathrm{d}\boldsymbol{S}'$, which is negative in the interior, implying an exchange of upward moving parcels within the plume for downward moving parcels outside. Near the boundary, this term is large and positive, suggesting that plumes gain momentum initially not due to their buoyancy anomaly, but due to the convergence of horizontal flow into jets directed away from the boundary. Without rotation, the pressure deceleration (about 1/4 of the buoyancy forcing) has little effect on the net acceleration which continues to increase over the lower half of the layer, until close to the end of the plume trajectory, when the pressure deceleration increases as plumes encounter the opposite boundary, and a more complete hydrostatic balance is achieved.

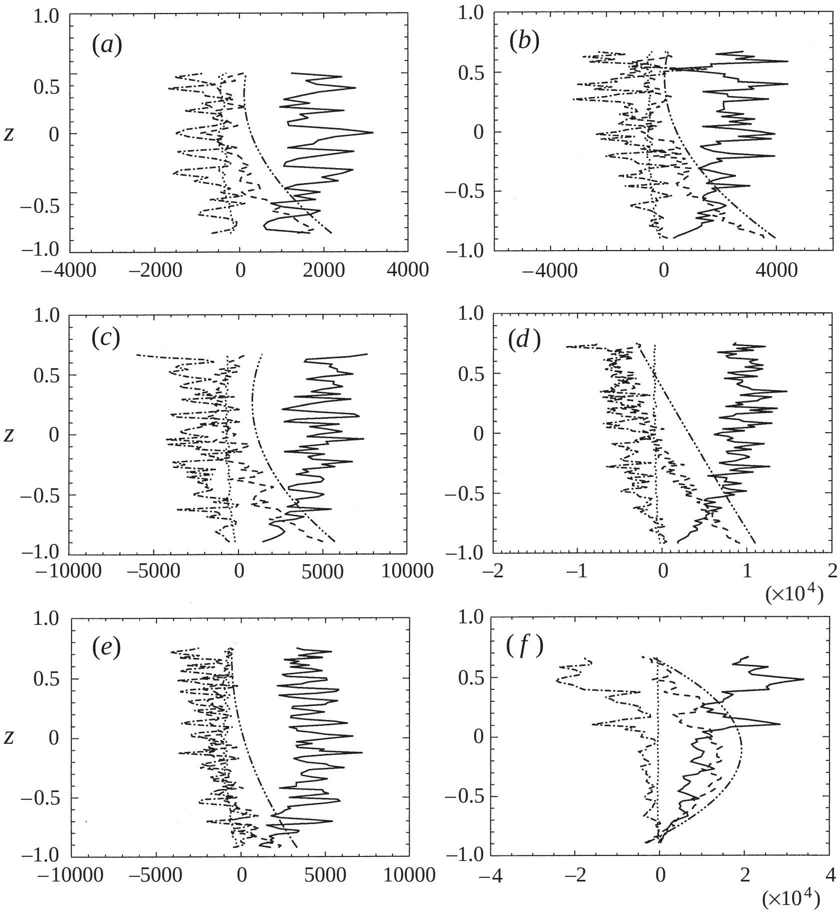

FIGURE 11. The components of the vertical momentum Lagrangian balance for the same simulations as in figure 10. Different terms are: dot-dash-dot line $= (\mathrm{d}/\mathrm{d}z)(V\overline{W^2}) \equiv (\mathrm{d}/\mathrm{d}t)(V\overline{W})$, dotted line $= V\nu\nabla^2\overline{W}$, solid line $= V\overline{g'}$, dash-dots line $= -V\overline{\partial P'/\partial z}$ and dashed line = residual = $(\mathrm{d}/\mathrm{d}z)(V\overline{W^2}) - V\nu\nabla^2\overline{W} - V\overline{g'} + V\overline{\partial P'/\partial z}$ which we equate with $\oint_S w v_e dS' - \oint_S w\mathbf{U}\cdot\mathrm{d}\mathbf{S}'$. All quantities are non-dimensionalized by κ^2.

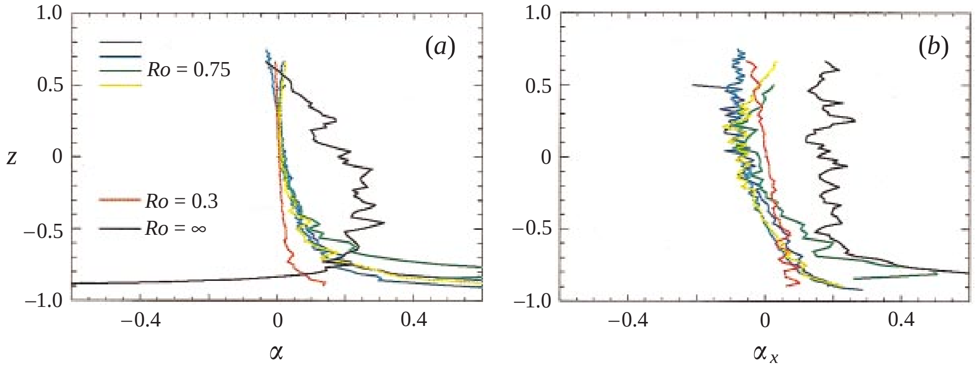

FIGURE 12. (a) The entrainment coefficient $\alpha = V_e/\overline{W}$ where $V_e = (\mathrm{d}/\mathrm{d}z)V\overline{W}/S$ and (b) the exchange coefficient $\alpha_x = U_x/\overline{W}$.

Implied entrainment and exchange coefficients

From the mass equation (2.12*a*) we can obtain an estimate of the mean entrainment velocity:

$$V_e = \frac{(\mathrm{d}/\mathrm{d}z)V\overline{W}}{S}. \tag{5.4}$$

We calculate α to assess the entrainment hypothesis:

$$\alpha = \frac{V_e}{\overline{W}}; \tag{5.5}$$

α defined in this way is shown plotted in figure 12(*a*) as a function of the plume position, for all simulations. The entrainment velocity ratio decreases rapidly and remains close to zero over the upper half of the volume for strong rotation, as shown by previous studies, while $\alpha > 0.1$ over most of the volume without rotation, close to that found for isolated plumes (Papanicolaou & List 1988).

Having found the entrainment velocity, we evaluate the relative contributions of entrainment and exchange to the heat budget by separating the residual term of the heat budget as follows. First, we assume that heat is entrained by the same effective entrainment velocity as mass, so that the heat entrainment term can be approximated as

$$\oint_S T v_e \mathrm{d}S' \approx \alpha \overline{W} S T_E = T_E \frac{\mathrm{d}}{\mathrm{d}z} V\overline{W} \tag{5.6}$$

where T_E is the entrained fluid temperature.

We approximate the exchange term similarly:

$$\oint_S T\boldsymbol{U}\cdot \mathrm{d}\boldsymbol{S}' \approx T_x u_x S, \tag{5.7}$$

where u_x is an exchange velocity scale, and T_x an exchange temperature scale. Since the surface-averaged velocity across the thermal boundary is zero from continuity, u_x represents an r.m.s. anomaly velocity across the boundary.

If we parameterize u_x in a similar manner to the entrainment velocity

$$u_x = \alpha_x \overline{W}, \tag{5.8}$$

we then have the residual in the heat equation (2.10) written as

$$\text{Residual} = \oint_S T v_e \mathrm{d}S' - \oint_S T\boldsymbol{U}\cdot \mathrm{d}\boldsymbol{S}' = T_E \frac{\mathrm{d}}{\mathrm{d}z} V\overline{W} + \alpha_x T_x \overline{W} S. \tag{5.9}$$

To solve for α_x we make suitable choices for T_E and T_x (the temperature difference between exchanged parcels of fluid): $T_E = T_0$, the horizontally averaged temperature, and $T_x = \overline{T} - T_0$.

Then

$$\alpha_x = \frac{1}{S}\frac{(\text{Residual} - T_0(\mathrm{d}/\mathrm{d}z)V\overline{W})}{((\overline{T - T_0}))(\overline{W})}. \tag{5.10}$$

Since the plume is warmer than its surroundings, we expect motion directed away from the plume centre to be associated with warm temperature anomalies, and motion toward the plume centre to be associated with cooler temperatures, a down-gradient lateral flux associated with negative values of both the exchange term and α_x. Figure 12(*b*) shows α_x calculated from (5.10); it is negative for all rotating runs, and of greater magnitude than the entrainment coefficient. Hence for the rotating runs, warm fluid

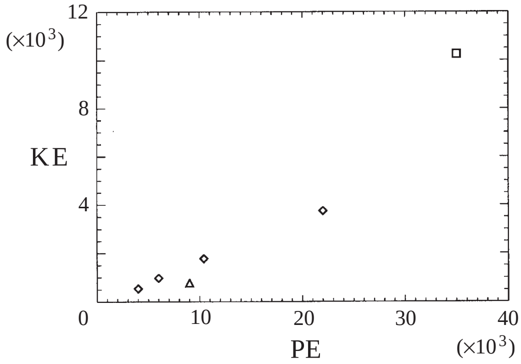

FIGURE 13. The maximum kinetic energy of the plume shown plotted against the maximum potential energy of the plume, for runs with $Ro_c = 0.75$ (diamonds), $Ro_c = 0.3$ (triangle) and $Ro_c = \infty$ (square).

from the plume is exchanged with cooler fluid from the exterior, resulting in a down-gradient flux which decreases the plume heat content. α_x has similar magnitude for all the runs with $Ro_c = 0.75$: $\alpha_x \approx -0.1$, and is independent of Reynolds number. For $Ro_c = 0.3$, α_x is slightly smaller.

Without rotation, there is a positive residual in the heat equation over most of the domain (figure 10*f*). If we assume that entrained fluid is at the mean ambient temperature, which is close to zero, this implies a positive exchange coefficient α_x (figure 12*b*), and a counter-gradient flux (hotter fluid moving into the plume, cooler fluid moving out of the plume). One explanation for this result is a 'buoyancy sorting' mechanism postulated previously in relation to cumulus convection (e.g. Hu 1997). If the fluid entrained into the plume has a considerable spread of temperatures, and the plume interior is not well-mixed, subparcels with less than the plume average temperature may be preferentially detrained, having insufficient buoyancy to continue ascending with the rest of the plume. Alternatively we may be incorrectly estimating the entrained heat by assuming the entrained fluid is at the average ambient temperature. If instead entrained fluid is substantially hotter than the mean ambient temperature (because for example, other hot plumes are combining to form larger hot plumes) then entrainment alone, without any counter-gradient flux due to mixing, could account for the increase in heat flux implied by the positive residual in the heat equation. In fact evidence described below suggests that individual hot plumes are combining as they ascend. We therefore favour the argument that entrainment is of hotter than average fluid for non-rotating plumes as a cause of the diagnosed $\alpha_x > 0$ rather than the buoyancy sorting mechanism.

The energy conversion ratio

To evaluate the net effect of the suppression of acceleration by pressure-gradient and mixing terms on the conversion of the potential energy of the buoyancy plume to kinetic energy, we define an energy conversion ratio

$$R_{KE} = \frac{\frac{1}{2}W_f^2 V_f}{g_i' V_i h}, \tag{5.11}$$

where W_f is the final parcel velocity, V_f is the final volume, g_i' is the initial buoyancy anomaly, V_i is the initial volume and h is the depth over which the parcel travels. Both the idealized thermal of Morton *et al.* (1956) and an isolated blob with no entrainment would have $R_{KE} = 1$, with all potential energy converted to kinetic energy. To evaluate this ratio for each run, we use the maximum $g_i' V_i$, which for the rotating runs is approximately constant over the volume interior. The peak value of $W^2 V$ is used for $W_f^2 V_f$. In both cases, the estimate is made after smoothing by fitting to a fourth-order polynomial. The volume depth is given by $h = 2$. In figure 13 $W_f^2 V_f$ is shown plotted against $g_i' V_i h$. Note that all $Ro = 0.75$ cases appear to lie on a straight line, corresponding to $R_{KE} = \frac{1}{6}$. The $Ro = 0.3$ case has a lower value of $R_{KE} = \frac{1}{9}$, while for $Ro = \infty$, $R_{KE} = \frac{1}{4}$. This reduction in R_{KE} as Ro decreases is in agreement with the reduced penetrative fluxes observed in low Rossby number penetrative convection (Julien *et al.* 1996*b*).

To summarize, we find the heat, momentum and mass budgets show little dependence on Rossby number, provided the Rossby number is small. Large differences are found between the rotating runs and the non-rotating example, but little difference between $Ro_c = 0.3$ and $Ro_c = 0.75$. The momentum boundary condition (no slip or free slip) also has no qualitative influence on the plume behaviour. This may seem surprising, since the magnitude of vorticity at the boundary is decreased by dissipation in the viscous boundary layer in the no-slip case, while vertical velocity away from the boundary layer is enhanced by Ekman pumping (Julien *et al.* 1996*a*). However, these factors influence the properties with which the plume is injected into the interior, but need not influence the dynamical balances affecting that plume as it crosses the convecting layer provided the plumes are in the same dynamical regime. The influence of Reynolds number is seen only in the diffusion terms $\nu V\overline{\nabla^2 W}$ and $\kappa V\overline{\nabla^2 T}$ which increase as Re decreases.

Our most significant result can be summarized as follows: at low Rossby numbers entrainment is replaced by exchange of properties (heat and momentum) between thermal and ambient fluid without any net change in mass flux, leading to a decline in both heat and momentum fluxes. This exchange may be parameterized by an exchange coefficient which depends on Rossby number and depth ($\alpha_x \approx -0.1$, in the centre of the volume when $Ro_l < 1$; $\alpha_x \geqslant 0$ if $Ro_l = \infty$) and is independent of Reynolds number. Non-rotating convection shows no such loss of buoyancy by mixing. Since many geophysical convection scenarios consist of ensembles of plumes where the turbulence is generated by the plumes themselves, this exchange parameter may form the basis for including plume interactions in rotating convection parameterizations. However we anticipate further studies may reveal more subtle dependence of α_x on Ro_c at low Ro_c values, hinted by the $Ro_c = 0.3$ results.

We propose that the mechanism for this mixing is plume–plume interactions. We have earlier shown that in rotating convection, plumes are associated with cyclonic vortices (Julien *et al.* 1996*a*). Similarly to two-dimensional vortex dynamics, these vortices interact with one-another, leading to vortex merger and straining events, and introducing a vigorous horizontal stirring. Figure 12 in Julien *et al.* 1996*a* shows the merger of three vortices associated with plumes. Filaments may be shed from plumes during a merger, or a plume may be strained and entirely mixed into the surroundings by the action of a neighbouring plume. Hence plumes are subjected to lateral mixing, induced by the cyclonic vorticity field of neighbouring plumes. In non-rotating convection, by contrast, there is no cyclonic vorticity field associated with plumes, and hence no enhanced lateral mixing. Note that while rotation suppresses expansion of the plume by entrainment because of angular momentum constraints on the motion, these constraints do not imply a lack of horizontal motion, but simply an upper limit on the horizontal length scales over which divergence from the plume can occur. Non-divergent horizontal motion, carrying parcels into and out of the

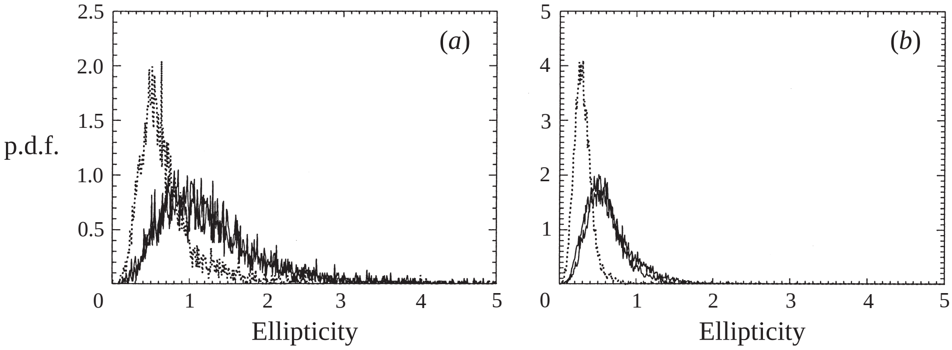

FIGURE 14. Probability density functions of the ellipticity $(a^2/b^2-1)^{1/2}$ where a/b is the ratio between axes lengths, for (*a*) $Ro_c = 0.75$, $(Ra - Ra_c)/Ra_c = 28.65$, no-slip boundary conditions, and (*b*) no rotation, $(Ra - Ra_c)/Ra_c = 1024$. Ellipticities are calculated for vertical vorticity (dotted line), temperature (solid line) and vertical velocity (dashed line). All good plumes at all vertical levels are included in the sample.

plume on subplume scales, is not suppressed but enhanced by rotation. Note that the azimuthally averaged plume structures shown in figure 2 may give the illusion that fluid only enters the plume at its base, and leaves at the top, because only azimuthally averaged fields are shown. The lateral mixing is provided by incursions into and out of the plume of equal magnitude, which therefore cancel when azimuthally averaged. (We quantify these distortions of the plume further below by examining the ellipticity of the plume shape.) In a subsequent article we will describe in detail actual events responsible for mixing fluid between plume and its surroundings.

Buoyancy acceleration in the interior is balanced to a large extent by pressure drag and momentum loss to the environment, reducing the acceleration, and resulting in a strong reduction in conversion of potential energy to kinetic energy in rotating plumes as compared with non-rotating plumes. Neither the Rossby-number-dependent mixing between plume and environment nor the Rossby-number-dependent reduction in acceleration are represented in classical plume models or in current plume-based parameterization schemes.

5.3. *Deviation from typical plume structure*

We have thus far examined only the azimuthally averaged composite plume, but azimuthal averaging may eliminate some important information about the typical plume shape: e.g. its ellipticity in the horizontal plane and its tilt from the vertical axis. We therefore calculate these quantities for individual plumes prior to azimuthal averaging or compositing. Since the previous parameter-space comparison has shown that all low Rossby number runs behave in a similar fashion, we will compare only one rotating and one non-rotating run.

5.3.1. *Ellipticity*

The ellipticity in the horizontal plane gives a measure of the deviation of the plume from an axisymmetric shape. Isolated plumes released from a point source are usually axisymmetric – ellipticity may be a result of the deformations induced by the turbulence surrounding a plume in the ensemble. As in the study of McWilliams (1990), we define ellipticity in the horizontal plane in the following manner: for each plume that passes the selection criteria, at the plume centre height we calculate the

2×2 matrix $\boldsymbol{M}$ whose components are

$$M_{i,j} = \frac{\displaystyle\int_A (q_i - q_{i,0})(q_j - q_{j,0})\mathrm{d}x\mathrm{d}y}{A}, \tag{5.12}$$

where $q_1 = x$, $q_2 = y$, (x_0, y_0) are the plume-centre coordinates and A is the area over which $F > F(x_0, y_0)/2.0$. The axes lengths a and b of the ellipse which best describes the area A are given by

$$\tfrac{1}{4}a^2 = \lambda_1, \quad \tfrac{1}{4}b^2 = \lambda_2, \tag{5.13}$$

where λ_1 and λ_2 are eigenvalues of $\boldsymbol{M}$. The ellipticity ζ is defined as

$$\zeta = \left(\frac{a^2}{b^2} - 1\right)^{1/2} = \left(\frac{\lambda_1}{\lambda_2} - 1\right)^{1/2}; \tag{5.14}$$

$\zeta = 0$ corresponds to a circular plume. We calculate ellipticities for the vertical velocity, vertical vorticity and temperature anomaly fields. Probability density functions (p.d.f.s) of ellipticity for the solution $Ro_c = 0.75$, $(Ra - Ra_c)/Ra_c = 28.43$ with no-slip boundary conditions are shown in figure 14(*a*). Note the peak in the p.d.f. at a value of $\zeta = 0.5$, corresponding to $a/b = 1.12$ for vorticity, and $\zeta = 1.0$ corresponding to $a/b = 1.4$ for vertical velocity and temperature. The high-ζ tail of the p.d.f. is broad, with a significant fraction of plumes having $\zeta > 2.0$, corresponding to $a/b > 2.25$. The vorticity is more localized than the other fields, and more axisymmetric. Similar behaviour is noted for all the other rotating runs. The non-rotating calculation shows very different behaviour, with the peak in ellipticity p.d.f. in the temperature and vertical velocity fields at the much smaller value of $\zeta = 0.5$. The p.d.f. declines rapidly from this peak, so that $\zeta = 2.0$ is very rare. Hence the temperature and vertical velocity anomalies of the plume structures in non-rotating convection are significantly more axisymmetric than those in strongly rotating convection. This concurs with the hypothesis that rotation, by introducing a strong vertical vorticity signature to the plume, causes the lateral shearing and straining of plumes, due to vortex–vortex interactions (Julien *et al.* 1996*a*). The vortices themselves resist straining deformations, but the temperature and vertical velocity anomalies associated with a plume have greater horizontal extent than the associated vortex. Hence they are more affected by deformations. Increases in ellipticity involve drawing plume fluid away from its centre and allowing ambient fluid closer to it. Seen in an azimuthally averaged framework, an increase in ellipticity reduces the magnitude of the anomaly within the plume volume and hence is interpreted as an exchange of properties within that volume.

5.3.2. *Tilt*

We calculate the average tilt of a plume by identifying its axis as a function of height from the velocity maximum. The total tilt is the ratio of the horizontal separation between upper-most and lower-most points to the vertical extent of the plume. In all cases the peak in the p.d.f. is at a tilt value less than 0.5, corresponding to an angle of $\pi/8.0$. The non-rotating case shows a similar distribution of plume tilt. This value of tilt is sufficient to generate an impression of vertical localization if a tilted columnar structure is azimuthally averaged, and hence we cannot determine from the azimuthally averaged structures whether an isolated parcel model is more appropriate than a plume connected to the source of buoyancy. However, the highest-amplitude plumes (in terms of heat flux or vertical velocity) have the lowest average tilt. Any

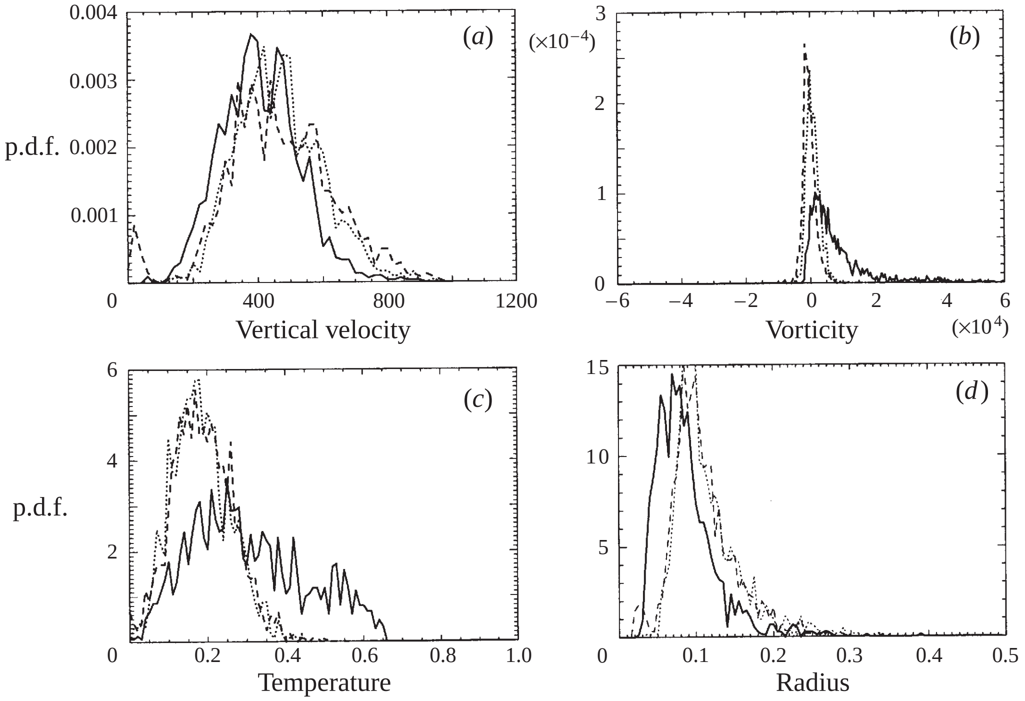

FIGURE 15. Probability density functions of (*a*) the vertical velocity, (*b*) the vertical vorticity and (*c*) the temperature anomaly at the centre of the individual plumes in the ensemble, and (*d*) the radius, as determined from the vertical velocity half-width. The plumes have been binned into those in (i) the lower third (solid line), (ii) the middle third (dotted line), (iii) the upper third (dashed line) of the volume.

deviations from vertical alignment or axisymmetry (as indicated by ellipticity) are in any case included in the exchange flux terms. Future work could account for the tilt of plumes by transforming plume quantities into a coordinate system aligned with the axis of the plume before azimuthally averaging. However, such transformations may introduce additional difficulties in compositing plumes with varying along-axis length.

5.4. *Plume ensemble statistics*

Thus far we have discussed the properties of the ‘typical plume’, a composite of all the members of the ensemble of ‘good plumes’ identified by the conditional sampling algorithm. A description of the transfers effected by the plume ensemble is not complete unless we know how representative this composite is of the members of the ensemble, and how much of the variability in the volume is captured by the ‘good plumes’.

5.4.1. *The variability within the ensemble*

Figure 15 shows the distributions of the temperature, vertical velocity and vorticity fields at the individual plume centres, classified into three groups determined by the plume-centre height. The p.d.f.s largely mimic those of the volume as a whole (Julien *et al.* 1996*a*). Most are fairly Gaussian, e.g. the vertical velocity at all levels and the temperature in the upper and middle thirds of the volume. The vorticity has a more exponential distribution in the middle and upper thirds, and a strongly

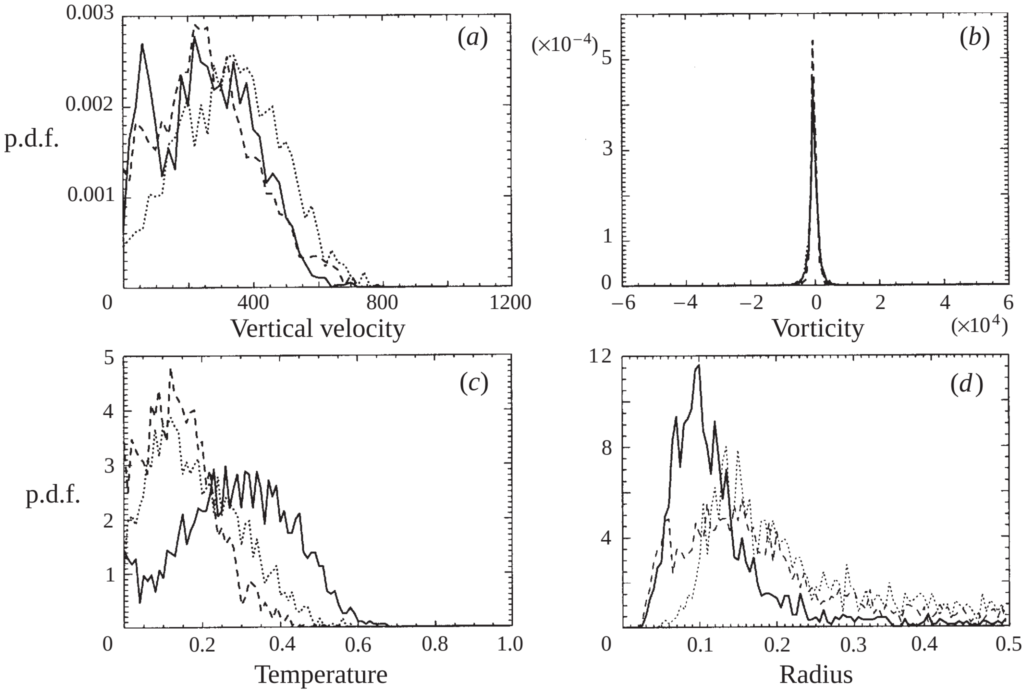

FIGURE 16. As figure 15 but for the non-rotating case, $Ro = \infty$.

skewed distribution in the lower third where the plumes originate (figure 15*b*). The temperature anomaly in the lower third is also skewed towards hotter plumes, but with a distribution which is closer to linear. (The temperature boundary conditions prevent the development of an arbitrarily large temperature anomaly.) The radius of the plume shows a non-Gaussian distribution, strongly skewed to larger radii at all vertical levels (figure 15*d*). Figure 16 shows the analogous quantities for the non-rotating case. The most important differences are the absence of a cyclonic skewness in the vorticity and no skewness toward high temperatures in the lower third of the layer (the p.d.f. is approximately symmetric for the non-rotating case). The distribution of radius shows an extended tail at large values, especially in the upper two-thirds of the volume. This suggests that without rotation entrainment may increase the size of a plume to very large values, while the constraints on rotating plumes bound the maximum size of a plume. Comparisons with p.d.f.s of quantities measured in a single axisymmetric plume (Papanicolaou & List 1988; Papantoniou & List 1989) show that the variability and tendency for extreme events is greatly increased in an ensemble compared to the time variations within a single plume.

5.4.2. *The area filled by plumes*

The simplest estimate of plume density would use the average number of good plumes identified by the conditional sampling algorithm. However, as shown in figure 17, these values are very noisy. Unlike the plume structure itself, the numbers of plumes identified depends very sensitively on the precise values of all the thresholds used in the plume extraction.

An alternative estimate of the number of plumes is made by first estimating the fractional area occupied by the upward plumes by identifying the area A_{plumes} where

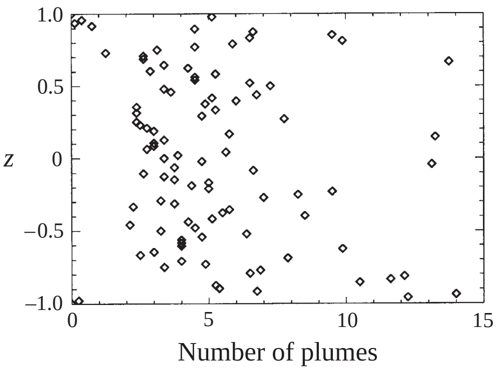

Figure 17. The average number of good plumes (i.e. satisfying all selection criteria) centred at each vertical level for $Ro_c = 0.75$, $(Ra - Ra_c)/Ra_c = 28.43$, and no-slip boundary conditions.

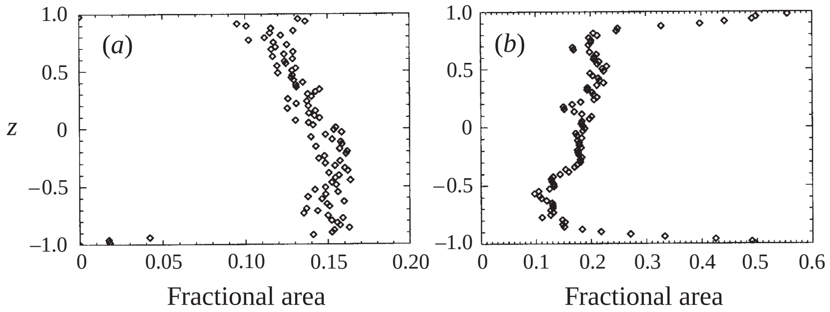

Figure 18. The fractional area occupied by vertical velocities greater than $W_0(z)/2.0$ where W_0 is the velocity at the centre of the composite plume located at height z for (*a*) $S = 28.43$, $Ro_c = 0.75$, no-slip; (*b*) $S = 1024$, $Ro_c = \infty$, no-slip.

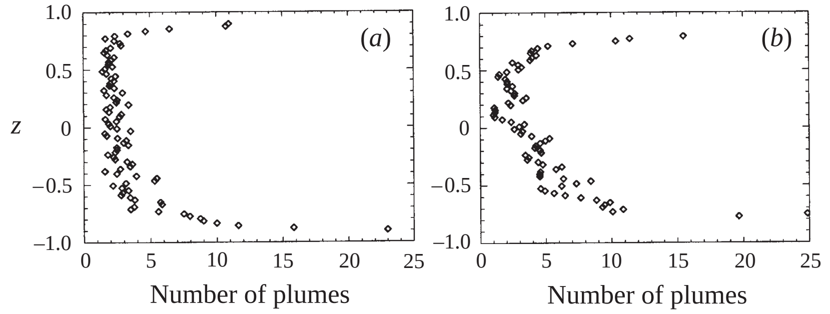

Figure 19. The equivalent number of plumes of radius $r(z)$ and vertical extent h (as identified from the half-width of vertical velocity of the composite plume) required to fill the area occupied by vertical velocities greater than $W_0/2.0$ for (*a*) $S = 28.43$, $Ro_c = 0.75$, no-slip; (*b*) $S = 1024$, $Ro_c = \infty$, no-slip.

vertical velocities are greater than half the plume-centre velocity at that height, i.e. $W(x, y, z) > W_0(z)/2$. This fractional area is shown in figure 18. For strong rotation, the fractional area occupied by the upward plumes decreases along the plume path, while without rotation the fractional area increases. To estimate the number of plumes from this fractional area, we first divide A_{plumes} by the area of a single plume πr^2. Then, since plumes have finite vertical extent, we eliminate overlapping plumes, and count

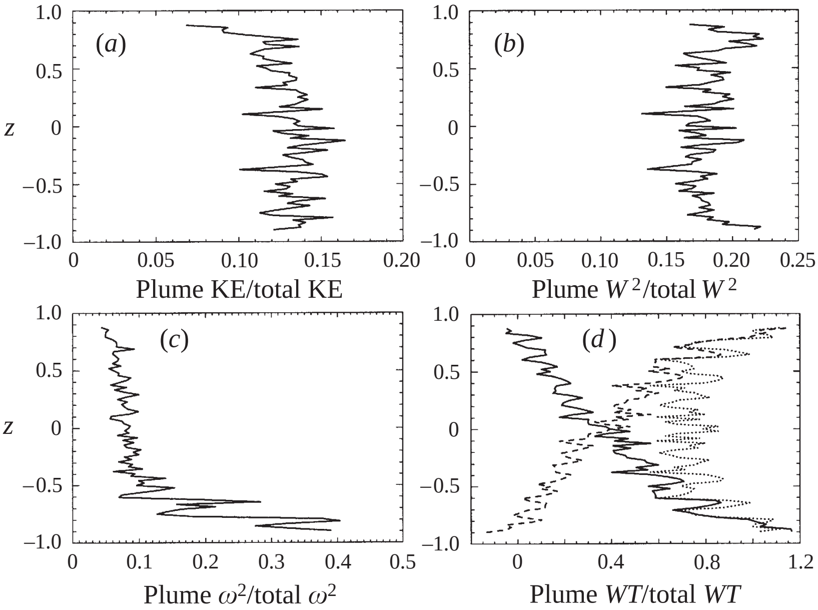

FIGURE 20. The fraction of (*a*) total kinetic energy, (*b*) vertical velocity variance, (*c*) vertical vorticity variance accounted for by the hot plumes, and (*d*) convective heat flux accounted for by hot plumes (solid line), cold plumes (dashed line), and all good plumes (dotted line), for run 1, $S = 28.43$, $Ro_c = 0.75$, no-slip. Note that the denominator in all cases is a function of height. The plume variances are calculated by (i) integrating the variance azimuthally and compositing over all good plumes, (ii) integrating over the volume of the good plumes, (iii) multiplying by the number of good plumes equivalent to the area occupied by $W > W_0/2$. The cold plume fraction in (*d*) is estimated by assuming symmetry between hot and cold plumes.

only those plumes centred at a particular level by dividing by the number of levels $h \times nz/(2L)$ occupied by a typical plume at a particular height, where h is the vertical extent of a plume, $2L$ is the height of the volume and nz is the number of vertical levels into which the volume is discretized. Then we obtain the number of plumes of average radius r and vertical extent h centred at a particular level: $N = A_{plumes}2L/(hnz\pi r^2)$ (figure 19). With strong rotation N declines very rapidly at first ($-1 < z < -0.4$), and thereafter more slowly ($-0.4 < z < 0.8$), suggesting two different mixing regimes. Early in the life of a plume smaller weaker structures are eliminated by the shearing due to strong vortices associated with adjacent stronger plumes, or merged into the larger plumes. Those plumes which survive then become subject to mixing with plumes emanating from the opposite boundary. Without rotation the equivalent number of plumes also decreases – the entrainment is sufficiently large that fewer and fewer plumes occupy more and more area, suggesting that much of the entrainment must involve engulfment of other plumes of the same sign. This concurs with our observation earlier of increasing plume heat content with height.

5.4.3. *The fractional variance accounted for by good plumes*

Having identified the properties of the hot plumes, and the approximate number of these plumes in the volume, we can evaluate the fraction of the total variances accounted for by these plumes. Shown in figure 20 are the fraction of (*a*) total kinetic energy $(w^2+u^2+v^2)/2$, (*b*) the vertical velocity variance w^2 and (*c*) the vertical vorticity variance ω^2 in the hot plumes for the strongly rotating case. The plumes account for

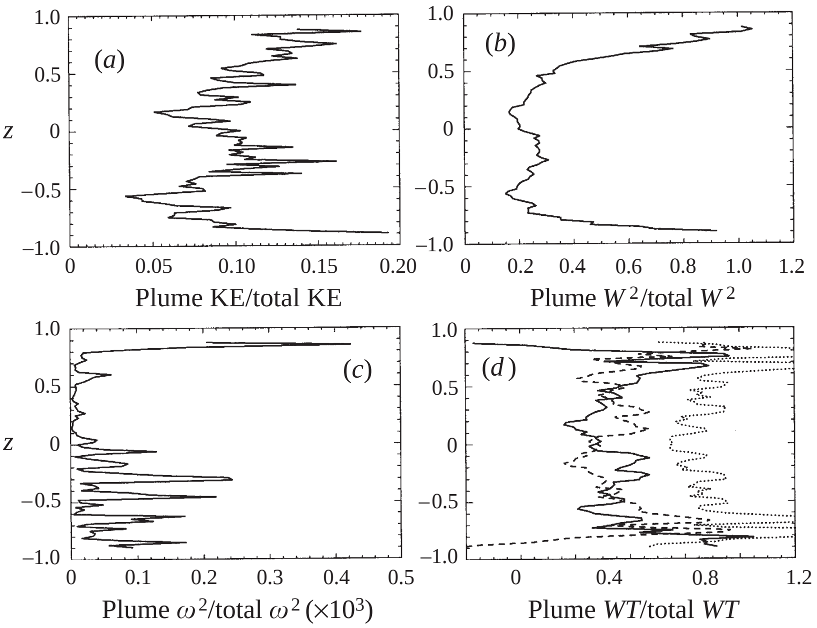

FIGURE 21. As for figure 20 but for run 6, $S = 1024$, $Ro_c = \infty$, no-slip.

a greater fraction of the vertical velocity variance than horizontal velocity variance. Horizontal velocity maxima are often outside the region bounded by $W > W_0/2$, and are therefore not accounted for by good plumes. Together with cold plumes, a total of close to 40% of the vertical velocity variance is accounted for by good plumes – a significant fraction. The plumes account for a large fraction of the vertical vorticity variance near the boundary layer (where the plumes are associated with strong vortices). In the interior however, filaments of vorticity no longer associated with plumes may exist, and the fractional variance of vorticity contained within the plumes is reduced.

Figure 20(*d*) shows the fraction of convective heat flux accounted for by hot plumes, cold plumes (assuming symmetry between hot and cold plumes) and the sum of hot and cold plumes. In the volume interior the plumes effect 80% of the heat transport, and closer to the boundaries an even greater fraction. However the fraction carried by plumes of a particular sign decreases approximately linearly along the plume path.

The plumes identified by the conditionally sampled composites carry out most of the heat transport in the volume, but account for a much smaller fraction of the total kinetic energy, since plumes are selected through a particular relationship between vertical velocity and temperature, implying positive heat flux localized within the plumes. No particular relationship between velocity fields is specified and much of the motion, especially horizontal motion, occurs outside the plume boundary. We do not expect these values to be very sensitive to the selection threshold values, since the most-coherent, highest-amplitude plumes are those associated with most of the vertical heat flux. Lowering the threshold would permit inclusion of more small weak plumes in the ensemble, not significantly altering the net heat flux.

Figure 21 shows analogous quantities for the non-rotating case. Again plumes account for a significant fraction of kinetic energy and heat flux. The plumes are not associated with a coherent vertical vorticity signal, and therefore account for little of the vertical vorticity variance. The most significant difference between the rotating and non-rotating cases is in the heat flux: in the non-rotating case the fraction of heat flux carried by upwardly moving plumes is approximately uniform over the interior. Hence there is no gradient in flux carried by plumes along the plume path.

6. Conclusions

We have extracted the typical hot plume structures of rotating Rayleigh–Bénard convection from numerical solutions using a conditionally sampled compositing technique, and examined their heat, mass and momentum balances, comparing with entraining thermal models and with a non-rotating solution. We find that, as for previous studies of rotating convection (Fernando *et al.* 1991; Jones & Marshall 1993; Maxworthy & Narimousa 1994; Helfrich 1994), the entrainment rate is rapidly suppressed after plumes leave the boundary layer, when the local Rossby number < 1 and plumes are in gradient-wind balance. The suppression of entrainment, and the more-or-less constant volume of the parcel thereafter, ensure that the plume volume is approximately constant over most of the layer. By contrast, the plume heat content is continually modified by mixing with the environment despite the absence of entrainment. Previous studies of rotating plumes assumed that if entrainment ceased, the parcel would be isolated from interaction with the environment – we show that this is not so. Instead we find that an open parcel model, such as that of Priestley (1953) applies. From the heat and mass budget we deduce the relevant mixing velocity $u_x = \alpha_x W$, and find $\alpha_x \approx -0.1$ at low Rossby numbers. By contrast without rotation $\alpha \geqslant 0$, so that no loss of buoyancy occurs. Since turbulence levels are equally high in rotating and non-rotating cases, we propose that the enhanced mixing in the rotating case must result from the greater plume deformations (indicated by high values of horizontal ellipticity) induced by vortex–vortex interactions in the rotating plume ensemble. The plume buoyancy loss in the rotating case results in a reduction in total plume buoyancy flux along the plume path in the rotating case, while it remains approximately constant along the plume path in the non-rotating case.

For low Rossby numbers, the parcel acceleration is initially greater than implied by the buoyancy forcing, due to convergence of flow near the boundary into the plume, but in the interior acceleration declines, as the buoyancy acceleration is balanced by a combination of loss of momentum due to mixing and a pressure gradient deceleration. The resulting conversion of potential energy to kinetic energy is reduced as Rossby number decreases.

A parameterization scheme based on an entraining thermal model requires several modifications to describe rotating plume ensemble convection:

(*a*) The entrainment coefficient is not a constant, but varies with depth and Rossby number, falling rapidly to close to zero in the strongly rotating cases, and remaining at about $\alpha \approx 0.2$ in the non-rotating case.

(*b*) In the absence of significant entrainment, mixing continues between environment and plume, resulting in loss of buoyancy and momentum from the plume, and modifying the surrounding fluid. This mixing can be parameterized by a mixing coefficient, which is approximately constant in the interior. A weak negative stratification (observed in numerous numerical simulations and laboratory experiments of rotating convection: Julien *et al.* 1996*a*, *b*; Klinger & Marshall 1995; Fernando *et al.* 1991) can only be maintained by detrainment of plume fluid, and mixing of this fluid into the environment.

(*c*) The suppression of acceleration by the combined pressure gradient anomaly across the plume and the mixing of momentum with the environment should be included if the correct conversion of potential to kinetic energy is to be obtained. While many atmospheric convection parameterizations do not explicitly include the vertical momentum budget, it is necessary if the parameterization scheme is to capture overshoot of the neutral buoyancy level and penetrative convection (Donner 1993). As shown, the efficiency with which plume potential energy is converted to kinetic energy depends on the Rossby number.

We find that the plumes identified here are the dominant mechanisms of heat transport across the volume, and within the plume ensemble, momentum, buoyancy and vorticity have distributions which mimic those of the volume as a whole. Hence a plume-based parameterization scheme which (i) includes the modifications identified here and (ii) represents the convecting elements by an ensemble with property distributions of the form identified here may provide a useful model of convective transports and mixing.

A later article will describe actual events responsible for the mixing during the life-cycle of individual plumes, and examine the time-dependent nature of the plume evolution in greater detail.

S.L. and J.M. received partial support from ONR grant N00014-95-1-0316. S.L. receieved partial support from ONR grant N00014-98-1-0165, and a NOAA Climate and Global Change postdoctoral fellowship, administered by the Universities Corporation for Atmospheric Research. J.M. received partial support from ONR grant N00014-98-1-0125. K.J. and J.W. are partially supported by NSF (ATM-9811938) and NASA (NAG5-4918) grants. Computations were performed at the Pittsburgh Supercomputing Center, supported by the NSF, under Metacenter Allocation MCA93S010P.

REFERENCES

Alves, J. O. S. 1995 Open-ocean deep convection: understanding and parametrization. PhD Thesis, University of Reading.

Arakawa, A. & Schubert, W. H. 1974 Interaction of a cumulus cloud ensemble with the large-scale environment. Part I. *J. Atmos. Sci.* **31**, 674–701.

Aubrey, N., Holmes, P., Lumley, J. L. & Stone, E. 1988 The dynamics of coherent structures in the wall region of a turbulent boundary layer. *J. Fluid Mech.* **192**, 115–173.

Ayotte, B. A. & Fernando, H. J. S. 1994 The motion of a turbulent thermal in the presence of background rotation. *J. Atmos. Sci.* **51**, 1989–1994.

Berkooz, G., Holmes, P. & Lumley, J. L. 1993 The proper orthogonal decomposition in the analysis of turbulent flows. *Ann. Rev. Fluid Mech.* **25**, 539–575.

Bush, J. W. M., Stone, H. A. & Bloxham, J. 1992 The motion of an inviscid drop in a bounded rotating fluid. *Phys. Fluids* A **4**, 1142–1147.

Castaing, B., Gunaratne, G., Heslot, F., Kadanoff, L., Libchaber, A., Thomae, S., Wu, X.-Z., Zaleski, S. & Zanetti, G. 1989 Scaling of hard thermal turbulence in Rayleigh–Bénard convection. *J. Fluid Mech.* **204**, 1–39.

Chandrasekar, S. 1961 *Hydrodynamic and Hydromagnetic Stability*. Oxford University Press.

Ching, C. Y., Fernando, H. J. S. & Davies, P. A. 1996 Interaction between multiple line plumes: a model study with applications to leads. *J. Phys. Oceanogr.* **26**, 525–540.

Deardorff, J. W. 1970 Convective velocity and temperature scales for the unstable planetary boundary layer and for Rayleigh convection. *J. Atmos. Sci.* **27**, 1209–1211.

Donner, L. J. 1993 A cumulus parameterization including mass fluxes, vertical momentum dynamics and mesoscale effects. *J. Atmos. Sci.* **50**, 889–906.

Emanuel, K. A. 1994 *Atmospheric Convection*. Oxford University Press.

Fernando, H. J. S., Chen, R.-R. & Boyer, D. L. 1991 Effects of rotation on convective turbulence. *J. Fluid Mech.* **228**, 513–547.

Fernando, H. J. S. & Ching, C. Y. 1993 Effects of background rotation on turbulent line plumes. *J. Phys. Oceanogr.* **23**, 2125–2129.

Fritsch J. M. & Chappell, C. F. 1980 Numerical prediction of convectively driven mesoscale pressure systems. Part I: convective parameterization. *J. Atmos. Sci.* **37**, 1722–1733.

Gregory, D. & Rowntree, P. R. 1990 A mass flux convection scheme with representation of cloud ensemble characteristics and stability dependent closure. *Mon. Wea. Rev.* **118**, 1483–1506.

Helfrich, K. R. 1994 Thermals with background rotation and stratification. *J. Fluid Mech.* **259**, 265–280.

Heslot, F., Castaing, B. & Libchaber, A. 1987 Transitions to turbulence in helium gas. *Phys. Rev.* A **36**, 5870–5873.

Hu, Q. 1997 A cumulus parameterization based on a cloud model of intermittently rising thermals. *J. Atmos. Sci.* **54**, 2292–2307.

Jones, H. & Marshall, J. M. 1993 Convection in a neutral ocean; a study of open-ocean deep convection. *J. Phys. Oceanogr.* **23**, 1009–1039.

Julien, K., Legg, S., McWilliams, J. & Werne, J. 1996*a* Rapidly rotating turbulent Rayleigh–Bénard convection. *J. Fluid Mech.* **322**, 243–273.

Julien, K., Legg, S., McWilliams, J. & Werne, J. 1996*b* Penetrative convection in rapidly rotating flows: Preliminary results from numerical simulation. *Dyn. Atmos. Oceans* **24**, 237–249.

Kain, J. & Fritsch, J. M. 1990 A one-dimensional entraining/detraining plume model and its application in convective parameterization. *J. Atmos. Sci.* **47**, 2784–2802.

Klinger, B. A. & Marshall, J. 1995 Regimes and scaling laws for rotating deep convection in the ocean. *Dyn. Atmos. Oceans* **21**, 227–256.

List, E. J. 1982 Turbulent jets and plumes. *Ann. Rev. Fluid Mech.* **14**, 189–212.

Lumley, J. L. 1971 *Stochastic Tools in Turbulence* Academic.

Maxworthy, T. & Narimousa, S. 1994 Unsteady deep convection in a homogeneous rotating fluid. *J. Phys. Oceanogr.* **24**, 865–887.

McWilliams, J. C. 1990 The vortices of two-dimensional turbulence. *J. Fluid. Mech.* **219**, 361–385.

Mellor, G. L. & Yamada, T. 1982 Development of a turbulence closure model for geophysical fluid problems. *Rev. Geophys.* **20**, 851–875.

Morton, B. R., Taylor, G. I. & Turner, J. S. 1956 Turbulent gravitational convection from maintained and instantaneous sources. *Proc. R. Soc. Lond.* A **234**, 1–23.

Narimousa, S. 1996 Penetrative turbulent convection into a rotating two-layer fluid. *J. Fluid Mech.*, **321**, 299–313.

Paluskiewisz, T. & Romea, R. D. 1997 A one-dimensional model for the parameterization of deep convection in the ocean. *Dyn. Atmos. Oceans* **26**, 95–130.

Papanicolaou, P. N. & List, E. J. 1988 Investigations of round vertical turbulent buoyant jets. *J. Fluid Mech.* **195**, 341–391.

Papantoniou, D. & List, E. J. 1989 Large-scale structure in the far field of buoyant jets. *J. Fluid Mech.* **209**, 151–190.

Priestley, C. H. B. 1953 Buoyant motion in a turbulent environment. *Austral J. Phys.* **6**, 279–290.

Schmidt, H. & Schumann, U. 1989 Coherent structure of the convective boundary layer derived from large-eddy simulations. *J. Fluid Mech.* **200**, 511–562.

Schumann, U. & Moeng, C.-H. 1991 Plume budgets in clear and cloudy convective boundary layers. *J. Atmos. Sci.* **48**, 1758–1770.

Tiedtke, M. 1989 A comprehensive mass flux scheme for cumulus parameterization in large-scale models. *Mon. Wea. Rev.* **117**, 1779–1800.

Turner, J. S. 1963 The motion of buoyant elements in turbulent surroundings. *J. Fluid Mech.* **16**, 1–16.

Turner, J. S. 1986 Turbulent entrainment: the development of the entrainment assumption, and its application to geophysical flows. *J. Fluid Mech.* **173**, 431–471.

Wilson, D. K. 1996 Empirical orthogonal function analysis of the weakly convective atmospheric boundary layer. Part I: eddy structures. *J. Atmos. Sci.* **53**, 801–823.

Yuan, Y. M. & Mokhtarzadeh-Dehghan, M. R. 1994 A comparison study of conditional-sampling methods used to detect coherent structures in turbulent boundary layers. *Phys. Fluids* **6**, 2038–2057.